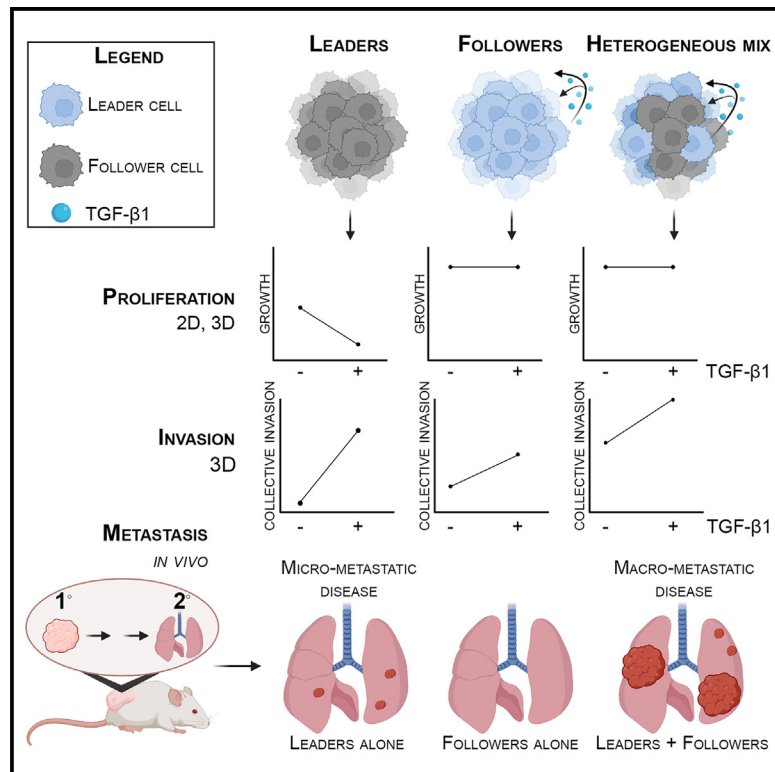


TGF- β 1-mediated intercellular signaling fuels cooperative cellular invasion

Graphical abstract



Authors

Tala O. Khatib, Brian A. Pedro,
Sergei Bombin, ..., Paula M. Vertino,
Janna K. Mouw, Adam I. Marcus

Correspondence

jmouw@emory.edu (J.K.M.),
aimarcu@emory.edu (A.I.M.)

In brief

Khatib et al. deconstruct an intercellular communication network required to drive collective invasion and tumor progression. They establish that actively invading NSCLC leader and follower cells communicate to establish a pro-invasive signature, sustain subpopulation proliferation, and drive tumor progression with TGFB1 identified as a key mediator.

Highlights

- Collectively invading NSCLC leader and follower subpopulations communicate via TGFB
- Without followers, isolated leaders exhibit quiescence in response to TGFB1
- Subpopulation cooperation sustains bulk population heterogeneity
- Both leaders and followers are required for macro-metastatic disease



Article

TGF- β 1-mediated intercellular signaling fuels cooperative cellular invasion

Tala O. Khatib,^{1,2,3} Brian A. Pedro,⁴ Sergei Bombin,^{2,5} Veronika Y. Matsuk,^{1,2} Isaac E. Robinson,^{1,2,6} Sarah F. Webster,^{1,2,3,7} Landon J. Marcus,⁸ Emily R. Summerbell,⁹ Gregory K. Tharp,¹⁰ Christina M. Knippler,² Pritha Bagchi,¹¹ Jeanne Kowalski-Muegge,¹² H. Rich Johnston,^{2,5} Homa Ghalei,^{3,7} Paula M. Vertino,¹³ Janna K. Mouw,^{1,2,*} and Adam I. Marcus^{1,2,3,14,*}

¹Department of Hematology and Medical Oncology, Emory University School of Medicine, Atlanta, GA 30322, USA

²Winship Cancer Institute of Emory University, Atlanta, GA 30322, USA

³Graduate Program in Biochemistry, Cell, and Developmental Biology, Emory University, Atlanta, GA 30322, USA

⁴Department of Pathology, Johns Hopkins School of Medicine, Baltimore, MD 21287, USA

⁵Emory Integrated Computational Core, Emory University, Atlanta, GA 30322, USA

⁶George W. Woodruff School of Mechanical Engineering, Georgia Institute of Technology, Atlanta, GA 30332, USA

⁷Department of Biochemistry, Emory University School of Medicine, Atlanta, GA 30322, USA

⁸Community Scientist, Atlanta, GA 30033, USA

⁹Office of Intramural Training and Education, The National Institutes of Health, Bethesda, MD 20892, USA

¹⁰EPC Genomics Core, Emory University, Atlanta, GA 30322, USA

¹¹Emory Integrated Proteomics Core, Emory University, Atlanta, GA 30322, USA

¹²Dell Medical School, University of Texas at Austin, Austin, TX 78712, USA

¹³James P. Wilmot Cancer Institute, University of Rochester School of Medicine and Dentistry, Rochester, NY 14642, USA

¹⁴Lead contact

*Correspondence: jmouw@emory.edu (J.K.M.), aimarcu@emory.edu (A.I.M.)

<https://doi.org/10.1016/j.celrep.2025.115315>

SUMMARY

Intratumoral heterogeneity drives cancer progression and influences treatment outcomes. The mechanisms underlying how cellular subpopulations communicate and cooperate to impact progression remain largely unknown. Here, we use collective invasion as a model to deconstruct processes underlying non-small cell lung cancer subpopulation cooperation. We reveal that collectively invading packs consist of heterogeneously cycling and non-cycling subpopulations using distinct pathways. We demonstrate that the follower subpopulation secretes transforming growth factor beta one (TGF- β 1) to stimulate divergent subpopulation responses—including proliferation, pack cohesion, and JAG1-dependent invasion—depending on cellular context. While isolated followers maintain proliferation in response to TGF- β 1, isolated leaders enter a quiescence-like cellular state. In contrast, leaders within a heterogeneous population sustain proliferation to maintain subpopulation proportions. *In vivo*, both leader and follower subpopulations are necessary for macro-metastatic disease progression. Taken together, these findings highlight that intercellular communication preserves tumor cell heterogeneity and promotes collective behaviors such as invasion and tumor progression.

INTRODUCTION

Tumor cell heterogeneity is a critical player in non-small cell lung carcinoma (NSCLC) progression and metastasis.¹ Approximately 75% of all early stage NSCLC tumors exhibit multiple clonal subpopulations, each with distinct driver mutations.² Factors such as genomic instability, therapy, and selective pressures from the tumor microenvironment contribute to this intratumoral heterogeneity, and correlate with disease progression, recurrence, and increased patient mortality.^{3–8} Additionally, substantial evidence suggests that solid tumors spread into the adjacent stroma via collective invasion, a cooperative process in which heterogeneous subpopulations move as a cohesive unit while maintaining cell-cell junctions.^{6,9–15}

To investigate the mechanisms underlying tumor cell heterogeneity, we developed a technique called spatiotemporal genomic and cellular analysis (SaGA),^{16,17} which allows for the isolation of live cells based on phenotypic criteria. Using SaGA, we previously isolated two NSCLC subpopulations based on their spatial localization within collectively invading packs. Leader cells, which are positioned at the leading edge, guide the pack; follower cells, comprising the pack majority, trail behind.^{17–21} These subpopulations are phenotypically stable, with distinct genetic, epigenetic, transcription, and metabolic signatures, and maintain spatial localization during 3D invasion when mixed together (with leaders positioned at the forefront and followers within the pack).^{10,11,17–22} While the observed heterogeneity and defined phenotypic roles within the collective



invasion pack suggest a cooperative interplay between these subpopulations, the modes and mechanisms of cooperation and subpopulation communication remain unclear.

To elucidate the interplay among cellular subpopulations, we integrated SaGA with single-cell RNA sequencing (RNA-seq) to isolate collectively invading cells from within a 3D context for comprehensive downstream analysis. Using various 2D and 3D *in vitro* strategies, along with *in vivo* mouse modeling, we analyzed subpopulation behaviors both in isolation and when recombined within various microenvironments. Our work revealed that heterogeneous cell-cycle states within the collective invasion pack drive distinct pathways related to invasion, secretion, translation, stress, and proliferation. We discovered a collective invasion-enabling signaling axis by which follower cells produce and secrete TGF- β 1 to orchestrate differential signaling networks across the collective invasion pack. Leader and follower subpopulations—cultured in isolation versus recombinant—exhibit differential translation, stress and proliferation signaling (*in vitro*) and metastatic potential (*in vivo*). Importantly, both leader and follower subpopulations are essential *in vivo* for the progression to macro-metastatic disease. Collectively, our findings indicate that tumor cell heterogeneity supports subpopulation maintenance and collective invasion to promote tumor progression.

RESULTS

Single-cell SaGA enables high resolution deconstruction of cell cycle dynamics within collective invasion packs

While we have previously demonstrated that NSCLC collective invasion packs are composed of distinct leader and follower cellular subpopulations, the specific mechanisms by which they cooperate remain to be elucidated.^{17–21} To this end, we isolated and profiled 3D live collectively invading cells by combining single cell RNA-seq with SaGA (Figures 1A and S1A). Using Seurat's cell cycle scoring method,²³ we observed that approximately 40% of the population resided in the non-cycling G1 phase, while the remainder of the cells resided within the proliferative S/G2/M phases (Figure 1B). Applying the t-distributed stochastic neighbor embedding (tSNE) analysis, we observed that G1 phase cells predominantly resided in CL1 and CL3, and S/G2/M phase cells resided in CL2 and CL4 (Figure 1C). Next, we determined that KI67 mRNA expression—a proliferation marker—could distinguish between non-cycling and actively proliferating cells with KI67-high expression largely associated with cells in S/G2/M phases (Figures 1D and 1E). Additionally, we confirmed that KI67-positive cells were heterogeneously dispersed throughout the invasion packs in the H1299, H1975, and H23 cell lines (Figure 1F). In contrast, most mitotically active cells were located near the rear of the invasion pack (Figures 1F and 1G).

Next, we performed gene set enrichment analysis (GSEA) to evaluate the gene expression signatures underlying non-cycling versus proliferative cells. Proliferative cells (KI67-high expression) upregulated typical pathways implicated in cell cycle progression, including chromosome segregation, nuclear division, and positive regulation of cell cycle process (Figure 1H). In

contrast, non-cycling cells (KI67-low expression) demonstrated upregulation of pro-migratory pathways such as tube and vasculature development, morphogenesis, and cell adhesion, as well as pathways related to secretion and cell stress response. Taken together, while 60% of the collectively invading cells are progressing through the cell cycle, the remaining cells are engaged in pathways that may contribute to pro-invasive behaviors.

Follower cells produce and secrete TGF- β 1 to elicit distinct responses across heterogeneous collectively invading subpopulations

We explored whether the transcriptomic heterogeneity observed in the non-cycling subpopulation may be driven by distinct SaGA-derived leader and follower subpopulation signatures (referred to here as leaders and followers). We leveraged previously defined leader and follower mutation profiles²¹ and determined enriched gene variants within our single cell dataset including six leader-specific mutation variants and eight follower-specific mutation variants with sufficient single cell sequence coverage (Figure 2A). We discovered near mutual exclusivity of these mutations within single cells with 54% of cells harboring one or more follower mutations and no leader mutations, and 35.1% of cells harboring one or more leader mutations and no follower mutations (Figures 2B and 2C). Only 4.5% of the cells displayed both leader and follower mutations, indicating a double-positive population. In contrast, 6.3% of the cells exhibited neither leader nor follower mutations, possibly due to insufficient coverage at these gene loci or an absence of any mutation variants. Interestingly, approximately one-third of the collectively invading population consisted of mutationally defined leader cells suggesting that, while the leading edge of the pack is predominantly piloted by leader cells, mutationally defined leaders may be capable of integrating spatially within the pack.

We assessed transcriptional expression of epigenetically regulated and binarily expressed leader and follower biomarkers, including MYO10 (leader) and IL13RA2 (follower).^{18,20,24,25} MYO10 and IL13RA2 transcript expression closely correlated with leader and follower mutationally-defined cells, resulting in an 87.4% complementary classification as either leader-like, follower-like, or those exhibiting both properties (Figure 2D). Next, we classified each cell in the tSNE plot by both KI67 and leader/follower (L/F) transcript expression status, which allowed for the inclusion of single cells with incomplete mutation loci coverage. We observed a cell cycle phase-dependent stratification with CL1 (follower like) and CL3 (leader like) predominantly featuring cells in the G1 phase (with KI67-low expression), and CL2 (follower like) and CL4 (leader like) consisting of cells in the S/G2/M phases (with KI67-high expression) (Figures 2E and 2F). These data suggest that both leader-like and follower-like subpopulations within the collective invasion pack include subsets of non-cycling and proliferative cells.

Further GSEA identified that both leader- and follower-like KI67-high expressing cells upregulated cell cycle progression related pathways, such as mitotic sister chromatid segregation and nuclear division (Figures S1B and S1C). Non-cycling leader-like cells mainly employed pathways linked to morphogenesis, cell matrix adhesion, tissue remodeling, and integrin-mediated signaling

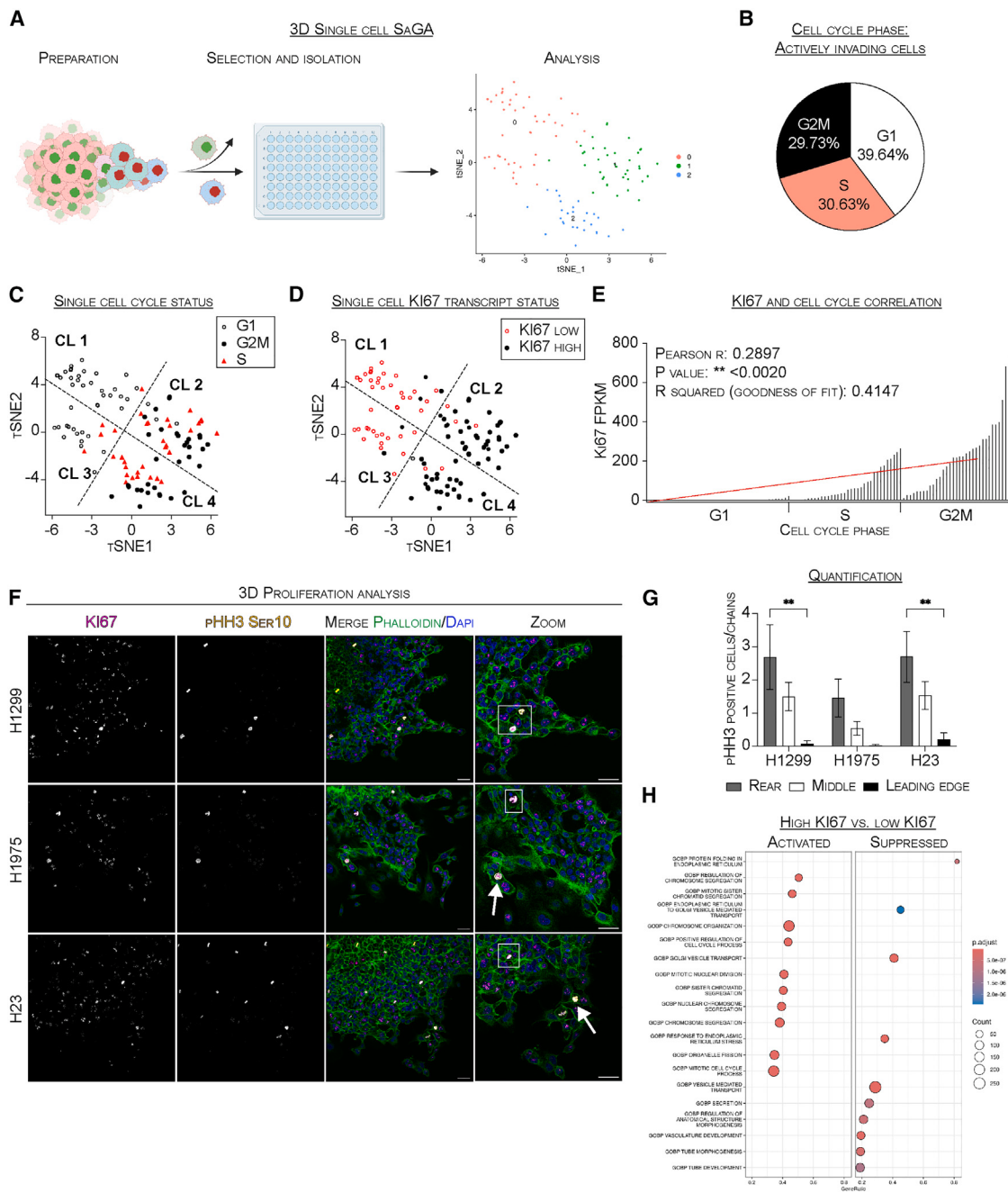


Figure 1. Single-cell SaGA enables high resolution deconstruction of cell cycle dynamics within collective invasion packs

(A) Single-cell SaGA graphical schematic. Created with [BioRender.com](#).

(B) Pie chart distribution of single cells categorized by cell cycle phase.

(C) tSNE visualization of cells clustered by cell cycle phase.

(D) tSNE plot showing KI67 mRNA transcript levels (fragments per kilobase of transcript per million mapped reads).

(E) Bar graph showing correlation analysis using Pearson's R coefficient. Pearson r two-tailed t test. Simple linear regression, goodness of fit r^2 value.

(F) Three-dimensional immunofluorescence of collective invasion packs. Phosphorylated histone H3 = pHH3. Scale bar, 50 μ m; $n = 2$.

(G) Bar graph quantifying (F). Data are represented as mean \pm SEM. Ordinary two-way ANOVA, Tukey's multiple comparisons test, with single pooled variance. $n = 2$, $N = 6$.

(H) GSEA dot plot comparative analysis. See also [Figure S1](#).

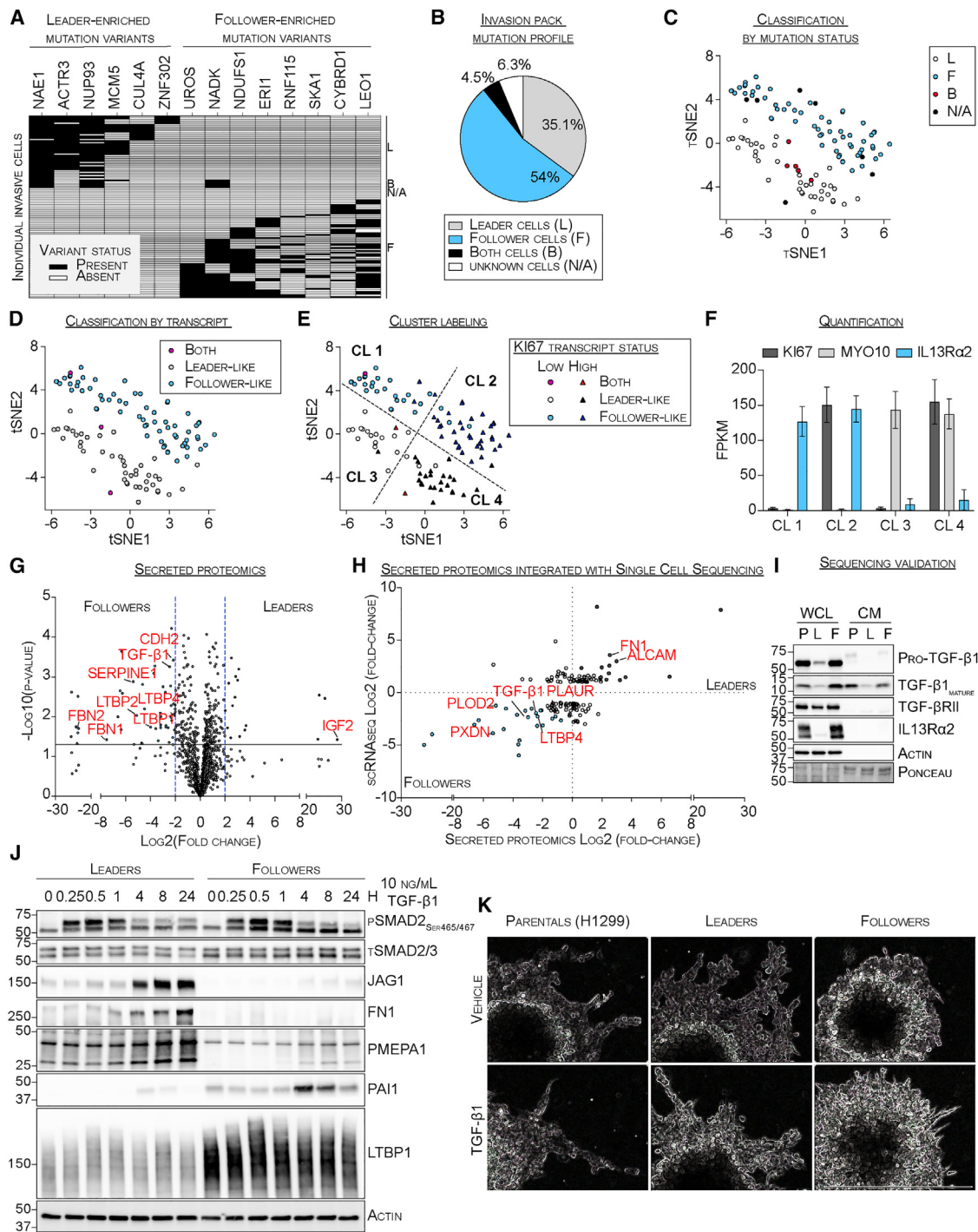


Figure 2. Follower cells produce and secrete TGF-β1 to elicit distinct responses across heterogeneous collectively invading subpopulations

(A) Mutation profile graph with rows representing a single cell classified as either a leader (L), both (B), unknown (N/A), or follower (F) cells.

(B) Pie chart categorizing single cells by their mutation profile.

(C) tSNE plot displaying clusters based on mutation profiles.

(D) tSNE plot displaying clusters based on mRNA transcript profiles.

(E) tSNE plot combining L/F and KI67 mRNA transcript status.

(F) Bar chart quantifying mRNA transcript levels by cluster. Data are represented as mean ± SEM.

(G) Volcano plot depicting differential leader and follower secreted factors assessed via proteomics. Blue dotted lines denote a 4-fold change, and the solid black line indicates a *p* value of <0.05. *n* = 4.

(legend continued on next page)

(Figure S1B). Non-cycling follower-like cells upregulated pathways related to protein trafficking, response to endoplasmic reticulum stress, and vesicle budding (Figure S1C).

Since all non-cycling cells upregulated secretion and vesicle mediated transport pathways, we performed proteomics on conditioned medium from leader and follower subpopulations to investigate potential communication pathways. A differential secretome analysis revealed that followers upregulate 50 of the detected 1,174 proteins, including transforming growth factor β 1 (TGF- β 1) and multiple TGF- β 1-related proteins (Figure 2G). In contrast, leaders upregulated 17 proteins including the growth factor IGF2, known to induce TGF- β 1 secretion.²⁶ Gene Ontology analysis highlighted the prominence of TGF- β 1 signaling within the follower conditioned medium, while analysis of the leader secretome revealed mechanisms consistent with cell migration (Figures S2A and S2B).

We then integrated our proteomics and single-cell transcriptomics data to assess proteins secreted during collective invasion (Figure 2H). TGF- β 1 and related proteins were enriched within the follower phenotype during collective invasion (Figure 2H). Interestingly, increased fibronectin (FN1) and ALCAM expression and secretion were observed in leader cells, both of which are known to respond to TGF- β 1.^{27,28} As expected, single cell RNA-sequencing identified key TGF- β 1-related genes differentially expressed between leader and follower subpopulations (Figure S2C). At the mRNA level, followers specifically upregulated TGF- β 1 and the TGF- β -related LTBP1/4, along with the canonical TGF- β targets SERPINE1/2 (PAI1/2). Leaders displayed elevated expression of multiple TGF- β -responsive genes including PMEPA1 and JAG1, along with various members of the inhibitor of DNA binding family (ID1, ID2). Across both subpopulations, similar levels of TGF- β 1 receptors (TGF- β R1, TGF- β R2), as well as the effector SMADs (SMAD2, SMAD3, and SMAD4) were observed. At the protein level, we validated that TGF- β 1 was highly produced and secreted in follower and parental populations compared with leader cells (Figures 2I and S2D). TGF- β R2 was expressed across all populations, while IL13RA2 was expressed within the parental and follower populations (Figures 2I and S2D). Next, we conducted a time course with recombinant human TGF- β 1 treatment and evaluated downstream targets. Leaders temporally upregulated JAG1, FN1, and PMEPA1 in response to TGF- β 1, while followers primarily upregulated PAI1 and LTBP1 (Figure 2J).

Next, we evaluated how follower-secreted TGF- β 1 regulates cooperative pack dynamics within a 3D microenvironment. We combined leader cells stably expressing a dendra2 green fluorescent protein with unlabeled follower cells (1:1 L/F mix) and treated with either exogenous TGF- β 1 or a vehicle control (Figure S2E). We confirmed that this recombined population recapitulates the spatial organization of the parental population, with leader cells predominantly at the leading edge, when treated with both vehicle and TGF- β 1. Across the parental, leader, and follower populations, we observed a reduction in invasive circu-

larity and an increase in number of chains following TGF- β 1 treatment, indicative of increased invasion (Figures 2K and S2F-S2H). Both parents and followers increased in invasive area in response to TGF- β 1, underscoring its facilitative role in driving collective invasion (Figure S2I). In contrast, TGF- β 1 decreased invasive surface area in leaders, while still increasing the number of invasive chains (Figures S2H and S2I). These findings demonstrate that the follower subpopulation predominantly produces and secretes TGF- β 1, and that leader and follower subpopulations distinctly respond to TGF- β 1 in both 2D and 3D microenvironments.

Follower-secreted TGF- β 1 promotes JAG1 and beta-catenin expression to support 3D cooperative collective invasion

We next assessed how TGF- β 1 downstream effector signaling regulates pro-invasive behaviors within isolated and recombined populations. All populations were treated with exogenous TGF- β 1 in a defined media; the TGF- β receptor II small molecule inhibitor, SB505124, was used to confirm the specificity and reversibility of TGF- β receptor-mediated downstream signaling. Following 48 h of TGF- β 1 treatment, all populations exhibited distinct expression of TGF- β 1 downstream targets to varying degrees (Figures 3A and S3A-S3C). In leaders, TGF- β 1 stimulated PMEPA1 and the JAG1/MYO10/FN1 axis,²⁰ with elevated PMEPA1, JAG1, MYO10, and FN1 levels (Figures 3A and S3A-S3C). In contrast, in the follower and parental populations, TGF- β 1 increased canonical TGF- β -target PAI1 expression (Figures 3A and S3A). The combined treatment with TGF- β 1 and SB505124 attenuated the observed effects of exogenous TGF- β 1 stimulation. Flow cytometry analysis revealed an almost 3-fold increase in cell surface JAG1 protein in leaders compared with followers when treated with TGF- β 1 (Figure S3D). qPCR analysis confirmed that TGF- β 1 stimulation induces JAG1 gene transcription across parental, leader, and follower cell populations (Figure S3E). In 3D, TGF- β 1 heterogeneously increased JAG1 expression, with cells on the leading edge expressing higher JAG1 levels in the parental and 1:1 L/F mixed population (Figures 3B, S3F, and S3G). Both leader and follower populations increased JAG1 expression across the invasive pack upon TGF- β 1 treatment, with leaders exhibiting higher JAG1 expression levels (Figures S3F and S3G).

When we further assessed the differential effects of TGF- β 1 on our subpopulations, we noted that—in 2D—acute and sustained TGF- β 1 stimulation resulted in a significant increase in active beta-catenin levels in leader cells and inhibited key regulators of beta-catenin turnover, GSK3a/b, while follower cells only modestly increased in GSK3a/b inhibition (Figures 3C and S3H-S3J). Via western blotting, we confirmed that under sustained TGF- β 1 stimulation, leader cells upregulate inhibitory phosphorylation of GSK-3b, resulting in a 2-fold increase of active beta-catenin levels (Figures 3C and S3H). In contrast,

(H) Dot plot integrating proteomics with scRNA-seq. Highlighted genes show a minimum of 2-fold change between leader and follower cells with a p value of <0.05 .

(I) Whole cell lysate (WCL) and conditioned media (CM) immunoblot analyses. $n = 3$.

(J) Immunoblot time-course analysis with TGF- β 1. $n = 3$.

(K) 3D spheroid invasion images with and without TGF- β 1. Scale bar, 500 μ m, $n = 3$. See also Figure S2.

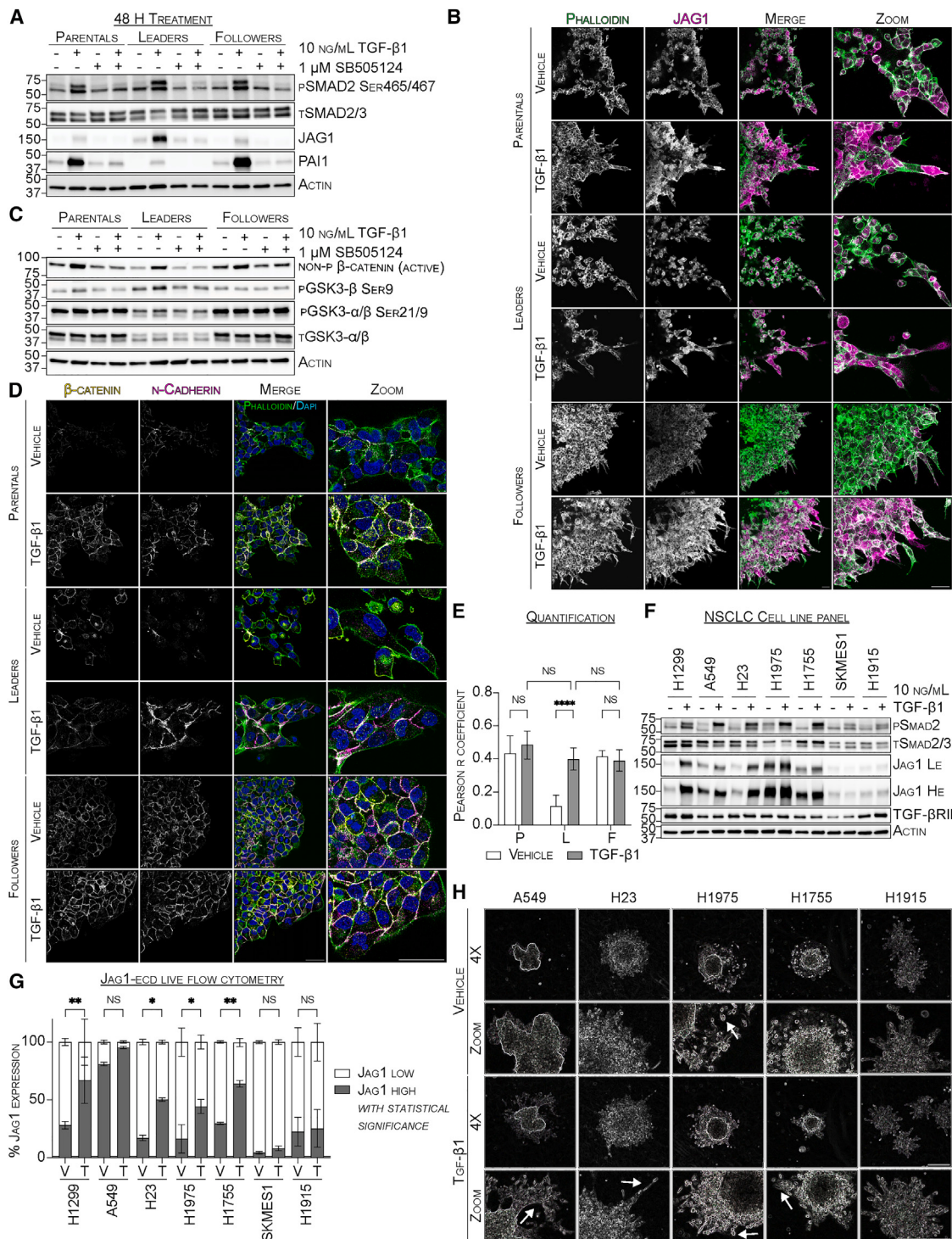


Figure 3. Follower-secreted TGF- β 1 promotes JAG1 and beta-catenin expression to support 3D cooperative collective invasion

- (A) Whole cell lysate (WCL) immunoblotting analysis treated with TGF- β 1 and/or SB505124. $n = 3$.
- (B) Three-dimensional immunofluorescence imaging of collective invasion packs with and without TGF- β 1. $n = 2$.
- (C) WCL immunoblot analysis treated with TGF- β 1 and/or SB505124. $n = 2$.
- (D) Three-dimensional immunofluorescence imaging of collective invasion packs with and without TGF- β 1. $n = 2$.
- (E) Bar graph quantifying Pearson's R correlation analysis in (D). Data are represented as mean \pm SD. $n = 2$, $N = 6$.
- (F) WCL immunoblot analysis with and without TGF- β 1. $n = 3$. Low exposure (LE), high exposure (HE).

(legend continued on next page)

followers consistently maintained high levels of phosphorylated GSK-3 α , regardless of TGF- β 1 stimulation, and exhibited a modest increase in active beta-catenin following TGF- β 1 treatment. In 3D, while beta-catenin and N-cadherin colocalized in the parental and follower-only invasion packs regardless of TGF- β 1 treatment, leader cells significantly increased cell:cell interactions upon TGF- β 1 stimulation, with N-cadherin co-localizing with beta-catenin at the adherens junctions (Figures 3D and 3E). These data suggest a cooperative interplay whereby follower-secreted TGF- β 1 inhibits GSK3 β activity in leader cells to promote cell-to-cell adhesion and cohesive pack formation.

Our published work found that a subset of NSCLC cell lines relies on JAG1 to drive invasion.²⁰ As such, we tested whether JAG1-mediated invasion is facilitated by TGF- β 1-orchestrated cooperative events. We assessed a panel of collective invasion competent NSCLC cell lines (H1299, A549, H23, H1975, H1755, SKMES1, and H1915) for the production and secretion of TGF- β 1 (Figures S4A and S4B). While intracellular TGF- β 1 were similar, the secreted extracellular fractions of TGF- β 1 varied across the NSCLC lines, with lower levels of mature TGF- β 1 secretion in A549, H23, H1975, and SKMES1 (Figure S4B). TGF- β 1 treatment resulted in an increase in SMAD2 phosphorylation across all cell lines examined, confirming the activation of canonical TGF- β 1 signaling (Figure 3F). JAG1 expression increased in response to TGF- β 1 in the H1299, A549, H23, H1975, and H1755 lines (TGF- β -sensitive lines). In contrast, the H1915 and SKMES1 cell lines (TGF- β -insensitive lines) did not upregulate JAG1 in response to TGF- β 1, suggesting that JAG1 expression may be TGF- β 1 independent under these experimental conditions. Using flow cytometry, H1299, H23, H1975, and H1755 showed elevated JAG1 expression within a specific subpopulation with TGF- β 1 treatment (TGF- β sensitive, JAG1 heterogeneous), mirroring the L/F subpopulation dynamic observed in the H1299 parental population (Figures 3G and S4C). In contrast, the A549 line demonstrated a nearly homogeneous increase in JAG1 expression (TGF- β sensitive, JAG1 homogeneous) upon TGF- β 1 stimulation. The SKMES1 and H1915 lines showed negligible JAG1 expression response to TGF- β 1 stimulation (TGF- β insensitive, JAG1 homogeneous).

Consistent with the H1299 line, a subset of TGF- β -sensitive lines (A549 and H23) increased invasive area and number of invasive chains, while reducing spheroid circularity in response to TGF- β 1 during 3D collective invasion (Figures 3H and S4D–S4F). While the TGF- β -sensitive H1975 cells did not show a notable change in circularity or number of chains, TGF- β 1 stimulation promoted an increase in the overall invasive area and a shift from a mix of collective and single cell invasion to predominantly collective invasion (Figures 3H and S4D–S4G). Further, in the TGF- β -sensitive H1755 line, TGF- β 1 treatment reduced both invasive area and circularity, shifting the invasive pattern from a primarily follower sheet-like invasion phenotype to distinct packs led by spatially defined leader cells (Figures 3H and S4D–S4F). There were no observed changes in invasive area, circularity,

or chain number in the TGF- β -insensitive H1915 cells (Figures 3H and S4D–S4F). These results demonstrate that, with TGF- β 1 treatment, multiple NSCLC cell lines heterogeneously upregulate JAG1 and increase collective invasion.

Leader and follower cooperation attenuates the TGF- β 1-induced reduction in leader cell proliferation

We previously identified cycling and non-cycling subsets within both leader and follower subpopulations in collective invasion packs (Figures 1 and 2); thus, we next explored the differential proliferation responses to exogenous TGF- β 1 across our populations both in isolation and recombined. After a 24 h time course with TGF- β 1 stimulation, the follower, parental, and 1:1 L/F mixed populations maintained robust proliferation (as indicated by pH3), while leader cell proliferation decreased over time (Figure 4A). This reduction in proliferation was paralleled with an increase in the cell cycle inhibitor p21 in leaders. After 48 h, TGF- β 1 further reduced proliferation in leaders with a nearly 5-fold reduction in pH3 and 1.5-fold increase in p21 levels (Figures S4H and S4I). Conversely, proliferation of the parental and follower populations remains relatively unchanged, with SB505124 mitigating observed TGF- β -related effects across all populations. Additionally, isolated leader cells significantly declined in proliferation over an extended 4-day treatment, while the proliferation rates of follower-only cells and the parental population remained largely unchanged (Figure 4B).

When we treated leaders with follower-conditioned medium, downstream TGF- β 1 signaling was activated, including the phosphorylation of SMAD2 and increased JAG1, PAI1, and activated beta-catenin protein levels; these effects were attenuated when treated with SB505124 (Figure 4C). Interestingly, unlike treatment with exogenous TGF- β 1, exposure to follower-conditioned medium did not result in reduced pH3 levels. As such, we investigated the impact of TGF- β 1 stimulation on leader cell proliferation within either the parental population or a 1:1 L/F mix compared with isolated leaders alone. We used flow cytometry to evaluate the subpopulation landscape (using IL13RA2 status to distinguish between leaders, IL13RA2-negative, and followers, IL13RA2 positive) and Ki67 status following TGF- β 1 treatment. In the isolated subpopulations, the non-cycling subpopulation (Ki67-low) decreased in followers in response to TGF- β 1, while the percentage of non-cycling cells increased in leaders (Figure 4D). When the subpopulations were mixed, leaders and followers exhibited minimal changes in cell cycle status following TGF- β 1 treatment, and there was no significant shift in the percentage of leader-like and follower-like cells within the parental population (Figure 4D). These data demonstrate that the leader subpopulation response to TGF- β 1 stimulation varies depending on the presence of the follower subpopulation. We next assessed how TGF- β 1 stimulation impacted subpopulation proliferation across our panel of NSCLC lines. Among the lines we previously identified as TGF- β -sensitive (Figures 3F, 3G and S4C), TGF- β 1 decreased proliferation in the H23, H1975,

(G) Bar graph quantifying flow cytometry treated with vehicle (V) or TGF- β 1 (T). Data are represented as mean \pm SEM. $n = 3$.

(H) Three-dimensional spheroid invasion images with and without TGF- β 1. $n = 3$. Scale bar, 500 μ m. All statistical analysis performed using ordinary two-way ANOVA, Sidak multiple comparisons test, with single pooled variance.

(B, D) Scale bar, 50 μ m. See also Figures S3 and S4.

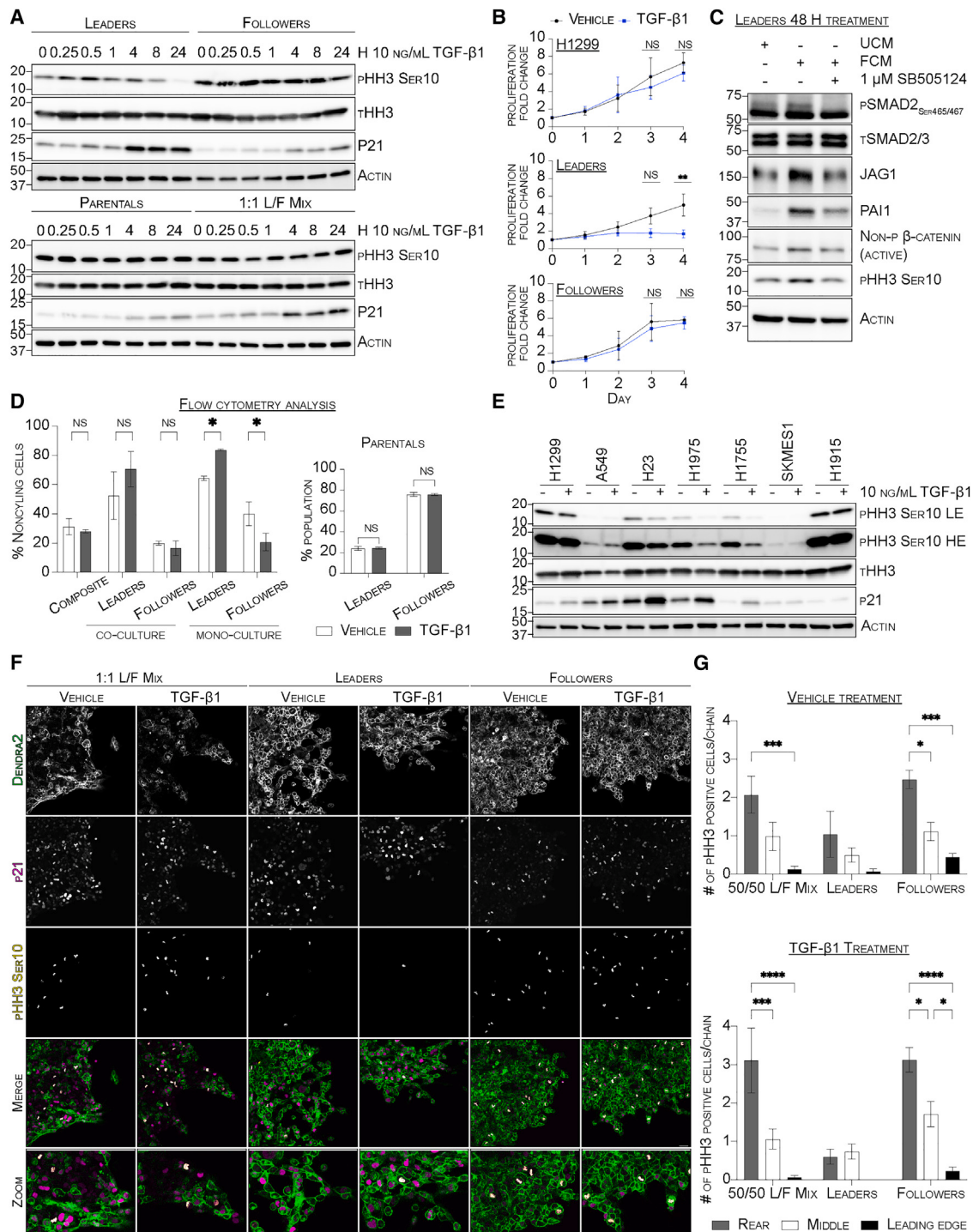


Figure 4. Leader and follower cooperation attenuates the TGF- β 1-induced reduction in leader cell proliferation

- (A) Whole cell lysate (WCL) immunoblot time-course analysis with TGF- β 1. $n = 3$.
- (B) Line graph quantifying proliferation over time with and without TGF- β 1. Data are represented as mean \pm SEM. $n = 3$.
- (C) WCL immunoblot analysis using unconditioned defined media (UCM) and follower conditioned media (FCM) with and without SB505124. $n = 3$.
- (D) Bar graph quantifying intracellular flow cytometry with and without TGF- β 1. Data are represented as mean \pm SD. $n = 3$.
- (E) WCL immunoblot analysis treated with and without TGF- β 1. $n = 3$.
- (F) Three-dimensional immunofluorescence imaging of collective invasion packs with and without TGF- β 1. Scale bar, 50 μ m, $n = 2$.

(legend continued on next page)

and H1755 lines after 48 h (Figure 4E). Conversely, minimal changes in proliferation were observed in the TGF- β -sensitive A549 cells, suggesting TGF- β -independent proliferation mechanisms. Similarly, TGF- β -insensitive lines (SKMES1 and H1915) showed minimal changes in proliferation in response to TGF- β 1. Last, the H1299 parental population exhibited minimal proliferation changes, confirming that leader cells comprise the minority of the population and changes to proliferation depends on the presence of follower cells.

When we evaluated proliferation differences in the isolated subpopulations and a 1:1 L/F mix during 3D collective invasion, we observed that, independent of TGF- β 1, proliferation was spatially regulated with actively proliferating cells predominantly localized toward the rear of the invasion pack (Figures 4F and 4G). In the 1:1 L/F mix and follower-only packs, the number of proliferating cells decreased within the middle and at the leading edge of the pack, while leaders generally exhibited reduced proliferation across the invasion pack (Figure 4G). Consistent with our 2D results, TGF- β 1 stimulation further suppressed proliferation in leader cell-only packs. In contrast, follower-only and mixed packs maintained high proliferation in the middle and rear. These data demonstrate the spatial distribution of proliferation within the pack with cells at the leading edge proliferating the least.

Leader and follower cellular cooperation manages stress within 2D and 3D micro-environments

Our lab and others have demonstrated that the LKB1-AMPK axis serves as a critical metabolic pathway in NSCLC, integrating cellular stress responses, energy homeostasis, and cell growth.^{29–33} When we assessed both LKB1 expression and AMPK activation in the parentals, leaders, and followers, we found that the isolated follower subpopulation expressed significantly higher LKB1 expression and activated AMPK compared with the isolated leaders (Figure S5A). To further explore this finding, we compared proliferation and the accompanying basal stress responses of our subpopulations to varying media conditions: 10% FBS media, defined media, or 100% RPMI media (Figures 5A and S5B). While leader cells maintained a similar proliferation rate to parental and follower cells when cultured in the nutrient-rich 10% FBS media for 48 h, their proliferation and cell-cycle progression were significantly reduced under both defined media and RPMI-only conditions. While the proliferation of the parental cells fluctuated modestly in response to different media, the follower cells maintained their basal proliferative capacity regardless of media condition. Negligible changes in total PARP and cleaved PARP were observed across all conditions, suggesting that the observed decreases in proliferation were not accompanied with cell death (Figure 5SB). Taken together, these data suggest that leader cell growth may be more sensitive to changes in the exogenous factors available within their micro-environment compared with follower cells.

Phosphorylation of ribosomal protein S6 (p-S6) correlates with the translation of proteins involved in proliferation and the cell cycle.³⁴ When we examined p-S6 within our populations in

response to varying media conditions (Figure 5A), we found that p-S6 was equivalent in media supplemented with 10% FBS. Consistent with the changes in proliferation, p-S6 levels were reduced in leader cells compared with followers under defined media conditions. Analysis of the cell stress response markers BNIP3, NDRG1, and HMOX1 showed that leaders differentially upregulate these factors compared with followers.^{35–37} We then evaluated how exogenous TGF- β 1 impacts stress markers, S6 translation, and proliferation under defined media conditions. Both the parental and follower-only populations maintained both proliferation and p-S6 levels, while showing negligible changes in stress markers in response to TGF- β 1 (Figure S5C). Conversely, isolated leader cells exhibited a marked decrease in proliferation, an increase in stress response signaling, and maintained reduced p-S6 levels upon TGF- β 1 treatment (Figure S5C). Again, we observed few to no changes in total or cleaved PARP across all conditions in response to TGF- β 1. These findings suggest that, while follower cells robustly proliferate across a range of media conditions, leader cells halt cell-cycle progression as a potential strategy to manage microenvironmental-induced stress.

Next, we explored whether co-culturing leader and follower cells could abrogate the leader cell stress observed under isolated conditions, which is exacerbated by TGF- β 1 stimulation. We compared isolated leader and follower subpopulations with heterogeneous populations (parental population and 1:1 L/F mix) stimulated with TGF- β 1. After 48 h, we used fluorescence-activated cell sorting to isolate and collect all subpopulations, including sorting leader and follower co-cultured subpopulations, for immediate lysis and subsequent downstream immunoblotting analyses (Figures 5B and S5D). While we observed minimal changes in JAG1 expression in isolated versus co-cultured populations, activated beta-catenin was increased in vehicle-treated co-cultured leaders compared with leaders in isolation (similar to Figure 4C). Co-cultured leader cells, whether within the parental population or the 1:1 L/F mix, exhibited increased proliferation and p-S6, regardless of TGF- β 1 stimulation. In contrast, leaders cultured alone showed reduced proliferation and translation, and increased markers of cell stress. Conversely, follower cells exhibited a slight reduction in proliferative capacity under co-culture conditions. Under 8-day TGF- β 1 treatment, isolated leader cells showed persistently elevated stress signaling, while co-cultured leaders maintained lower levels of stress response signaling (Figures 5C and S5E). Thus, while isolated leaders exhibit signs of cellular quiescence in response to cell stress, the presence of follower cells, or follower supplied factors, reduced stress signaling and facilitated leader cell proliferation.

When we assessed how our subpopulations—separately and re-combined—regulated S6 translation during 3D collective invasion, we found that cells at the leading edge of collective invasion packs, whether in the 1:1 L/F mix or leaders alone, express elevated p-S6, independent of TGF- β 1 (Figure 5D). This result stands in contrast with isolated leaders in 2D environments, where S6 phosphorylation is significantly lower compared with

(G) Bar graph quantifying the number of pH3-positive cells in (4F). Data are represented as mean \pm SEM. Ordinary two-way ANOVA, Tukey's multiple comparisons test, with single pooled variance. $n = 2$, $N = 5$. (B, D) Ordinary two-way ANOVA, Sidak multiple comparisons test, with single pooled variance. See also Figure S4.

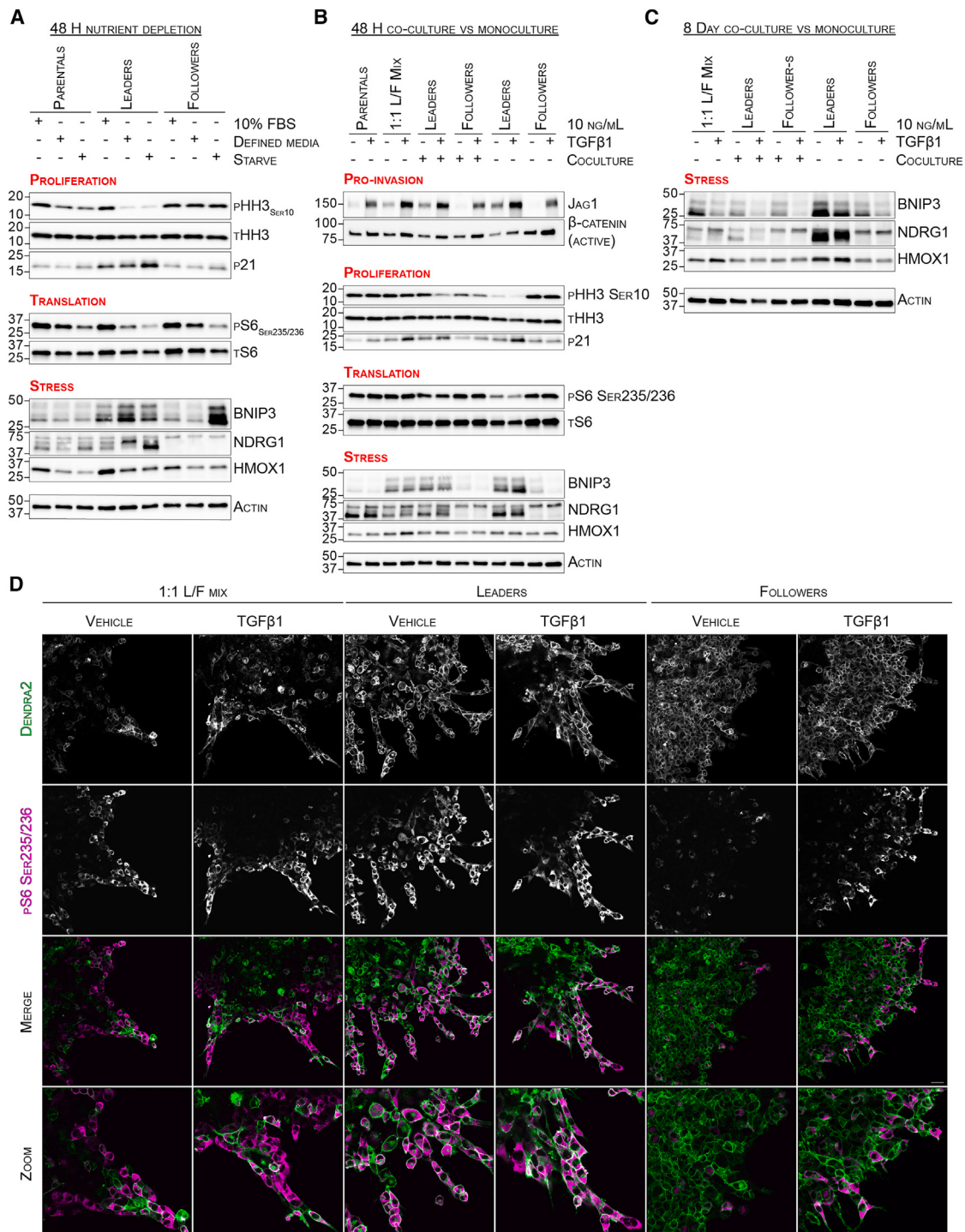


Figure 5. Leader and follower cellular cooperation manages stress within 2D and 3D micro-environments

(A) Whole cell lysate (WCL) immunoblot with varying media conditions. $n = 3$.

(B) WCL immunoblot analysis with and without TGF- β 1. $n = 2$.

(C) WCL immunoblot analysis with and without TGF- β 1. $n = 2$.

(D) Three-dimensional immunofluorescence imaging of collective invasion packs with and without TGF- β 1. Scale bar, 50 μ m, $n = 2$. See also Figure S5.

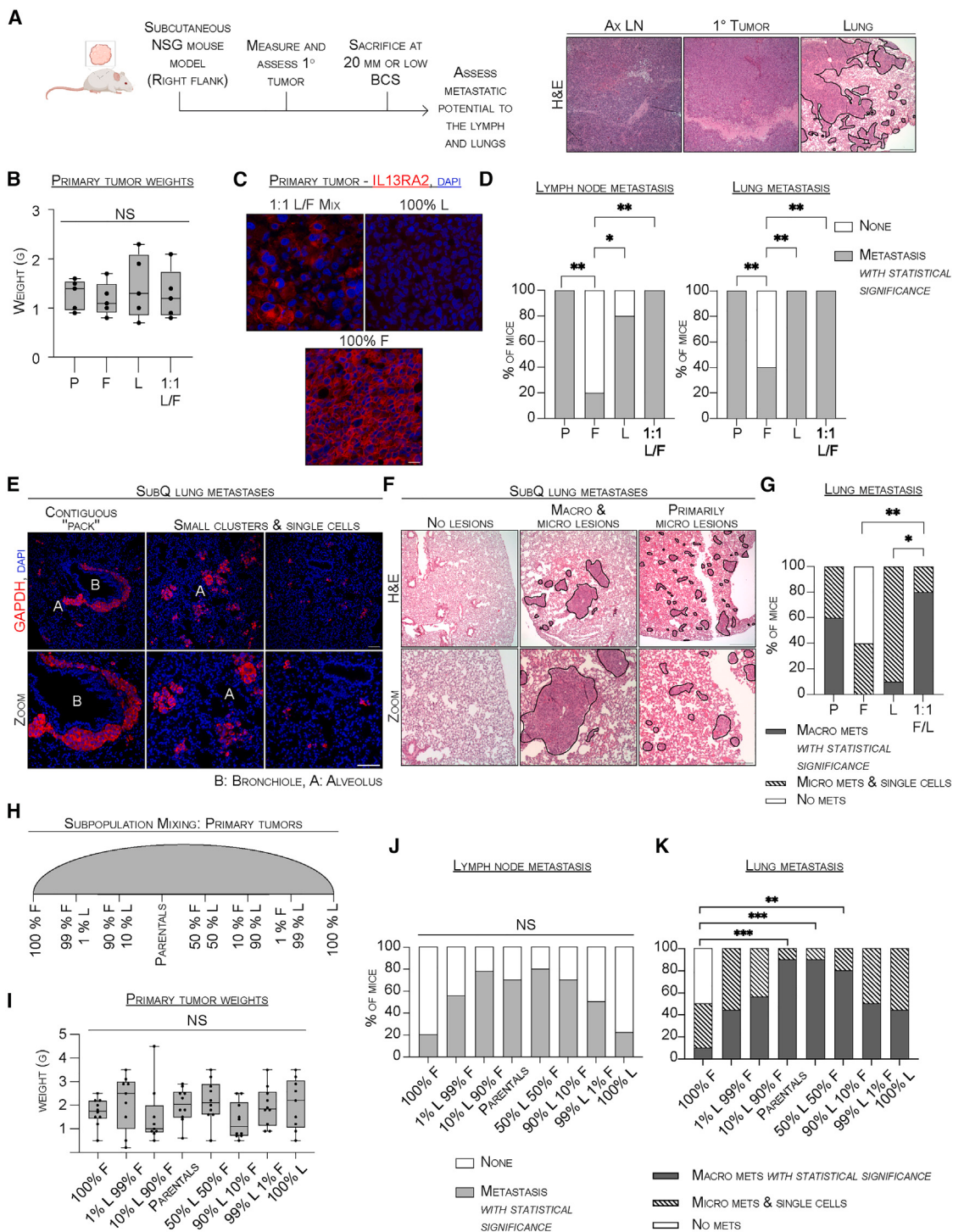


Figure 6. Leaders and followers in combination enhances tumor progression and metastatic disease in vivo

(A) In vivo mouse modeling schematic and Hematoxylin and eosin (H&E) stained sections. BCS, body condition score. Scale bar, 500 μm. Created with BioRender.com.

(B) Quantification of the primary tumor mass at experimental endpoint. Parental (P), leader (L), follower (F), and recombined mix (1:1 L/F). n = 5.

(C) Two-dimensional immunofluorescence of tissue sections. n = 5. Scale bar, 50 μm.

(D) Bar graph quantification. n = 5.

(E) Two-dimensional immunofluorescence of tissue sections. n = 5. Scale bar, 100 μm.

(F) Representative H&E lung metastases by lesion size. Scale bar, 500 μm.

(legend continued on next page)

parental and follower populations. Additionally, TGF- β 1 treatment increased p-S6-positive cells within the 1:1 L/F mixed population, with minimal impact on the p-S6 levels in isolated leader cells. Vehicle-treated follower cells demonstrated low p-S6 levels in 3D, contrasting with their p-S6 expression in 2D. However, TGF- β 1 treatment increased follower cell p-S6 levels at the leading edge, aligning with the levels observed in leader and recombined populations. Moreover, these results suggest that cooperation between distinct subpopulations may support subpopulation growth, population maintenance, and collective invasion to contribute to tumor progression.

Leaders and followers in combination enhances tumor progression and metastatic disease *in vivo*

Given that leader cells more effectively manage stress and proliferation when co-cultured with follower cells, we investigated how these populations respond within an *in vivo* microenvironment. The composite parental and 1:1 L/F mix populations as well as the individual subpopulations were subcutaneously injected and euthanized as they reached experimental endpoint (based on primary tumor burden) (Figure 6A). All groups, both isolated and composite populations, formed primary tumors at 100% (Figure 6B). The presence of leader and follower subpopulations were confirmed in the primary tumors by staining with the follower marker IL13RA2 (Figure 6C). As expected, follower-only tumors stained positive for IL13RA2 and leader-only tumors stained negative for IL13RA2; heterogeneous staining was evident in the composite tumor populations.

Metastases were observed to the axillary lymph node and the lungs. Lymph node involvement varied across experimental groups; while the rate of involvement was 100% in the composite populations and 80% in the leader-only population, only 20% of the follower-only primary tumors metastasized to the lymph node (Figure 6D). Similarly, lung metastasis occurred at 100% in the parental, 1:1 L/F mix, and the leader-only groups, but only 40% in the follower-only group (Figure 6D). Taken together, while all populations could establish primary tumors of equal burden, the composite and leader-only groups exhibited greater metastatic potential compared with the follower-only group.

Using a human-specific GAPDH antibody to detect secondary lesions in the lung, we detected singular cells and small lesions with a diffuse tissue distribution, as well as lesions with a contiguous distribution, suggesting the establishment of cohesive packs (Figure 6E). The lung involvement was classified into three categories: no lesions, single cells or micro-metastatic lesions (defined as ≤ 20 cells), or macro-metastatic lesions (defined as >20 cells within a cohesive lesion) (Figure 6F). While the proportion of mice bearing lung metastases from the leader-only primary tumors was similar to that of the parental and 1:1 L/F mix tumors, the sizes of the metastatic lesions varied significantly. The parental and 1:1 L/F recombined populations presented

with a mixture of single cells, micro-metastatic lesions, and macro-metastatic lesions. In contrast, the leader-only group primarily presented with single cells and micro-metastatic lesions (Figure 6G). The follower-only group exhibited low metastasis to the lung, with involvement limited to a few single cells and micro-metastases in a subset of mice.

Subsequently, we conducted an *in vivo* dilution series, using a range of population ratios from 1% to 99% L:F, to assess how the proportion of leader to follower cells influences the development of macro-metastatic disease (Figure 6H). Consistent with the previous experiment, all groups formed primary tumors at 100% (Figure 6I). We observed a dose-dependent response in metastatic burden to the axillary lymph nodes and lungs (Figures 6J and 6K). As the proportion of leader cells increased from 1% up to the levels present in the parental and the recombined populations, there was a corresponding increase in metastatic burden. However, when the percentage of leader cells exceeded 50% and approached the 90%–100% range, we observed a dose-dependent decrease in metastasis. Notably, the highest lung metastatic burden occurred in the parental population and the 1:1 L/F mix, suggesting the establishment of a cellular subpopulation landscape within the parental population advantageous for tumor progression.

Metastatic leader-only cells display a quiescent cellular phenotype

To confirm the presence of leader and follower cells in the secondary site lung microenvironment, we stained the lung tissues using the follower-specific marker, IL13RA2, and the leader-enriched, TGF- β 1-responsive marker, JAG1. Lung lesions resulting from leader-only primary tumors, which were mostly single cells and micro-metastases, were 100% JAG1 positive; mice bearing follower-only tumors exhibited a marked absence in IL13RA2 staining in the lungs, indicative of few to negligible cells present (Figure 7A). Within both the parental and 1:1 L/F mixed populations, both leaders and followers reached the lung secondary site. When we assessed the single cell and micro-metastatic lesions in the 1:1 L/F mixed group, we found that they were predominantly JAG1-enriched, indicating a leader-like cellular phenotype, without accompanying IL13RA2-positive follower cells. Taken together, these findings suggest that the lack of macro-metastatic lesions resulting from leader-only primary tumors may be due, in part, to the absence of follower cells.

We next investigated whether leader micro-metastatic and single cell lesions exhibited reduced proliferation and elevated stress, similar to isolated leaders *in vitro* (Figure 7B). In the leader-only group, we observed Ki67-low and p21-high expression, indicative of reduced cellular proliferation and cell-cycle arrest under isolated conditions. Further, phosphorylated EIF2 α , a negative translation regulator, revealed increased phosphorylation levels in the leader-only single cells and micro-metastatic

(G) Bar graph quantification. mets, metastases. $n = 5$.

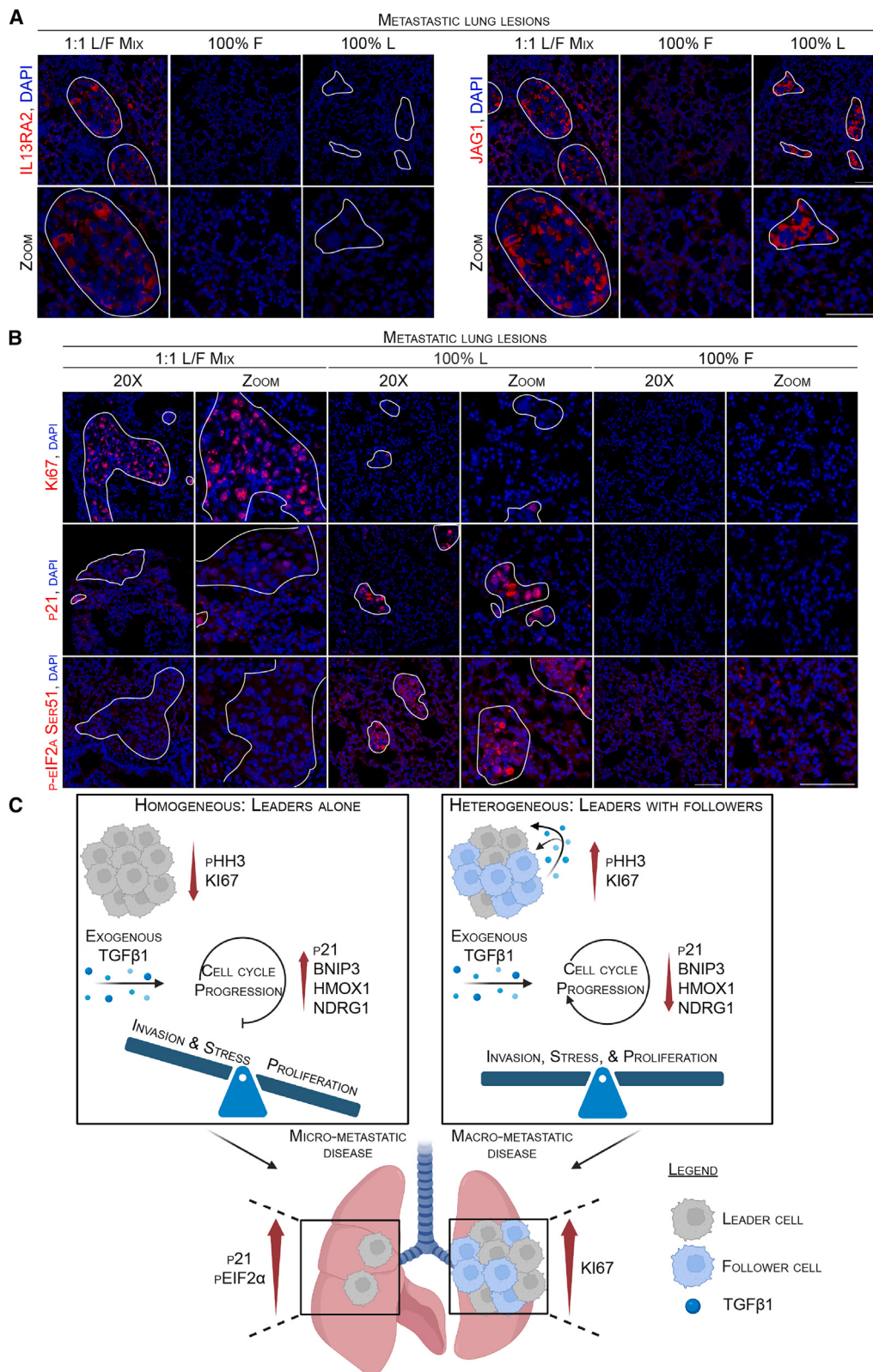
(H) Primary tumor dilution series schematic.

(I) Quantification of the primary tumor mass. $n = 9$ or 10.

(J) Bar graph quantification. $n = 9$ or 10.

(K) Bar graph quantification. $n = 9$ or 10.

All statistical analysis performed used ordinary two-way ANOVA, Sidak multiple comparisons test, with single pooled variance.



(legend on next page)

lesions, indicative of increased stress signaling and translation inhibition. Conversely, macro-metastatic lesions in the 1:1 L/F recombined population were proliferative, as indicated by Ki67-high and p21-low expression. Smaller micro-metastatic lesions from the same group were Ki67-negative and p21-positive, suggesting reduced proliferation capacity. We observed decreased EIF2 α phosphorylation in the 1:1 L/F macro-metastases, suggesting active translation and reduced stress signaling. Taken together, the leader-only secondary site lesions display a non-proliferative quiescent cellular phenotype—similar to the quiescent phenotype observed *in vitro*—characterized by Ki67-low expression and inhibited protein synthesis.

DISCUSSION

In this study, we combined single-cell SaGA, *in vitro* 2D and 3D approaches, and *in vivo* mouse modeling to investigate whether communication and cooperation between heterogeneous subpopulations supports NSCLC invasion and tumor progression. We performed a multiscale assessment across these various platforms, from single cell to subpopulation to heterogeneous population, to establish that subpopulations cooperate to maintain heterogeneity, reduced stress signaling, and ultimately drive tumor progression (Figure 7C).

Our *in vitro* findings are corroborated *in vivo*, where we demonstrate that both subpopulations are required for macro-metastatic disease. These findings suggest critical roles for both subpopulations in facilitating tumor progression. Leader cells are adept invaders that can navigate the stages of the metastatic cascade to pilot into secondary site tissues. However, they fail to sustain the proliferative capacity necessary for colonization, leading to the predominant formation of quiescent micro-metastatic lesions. Conversely, follower cells are less adept at invasion and, therefore, may be less likely to navigate the invasive stages of the metastatic cascade in the absence of their pro-invasive leader counterpart. However, when leader and follower cells comprise a heterogeneous tumor population, they cooperate to promote tumor progression and elicit a metastatic advantage through successful colonization and proliferation at secondary sites. Notably, the ability for leaders in isolation to transition into a quiescent state highlight that—while they may lack the resources to mitigate stress independently—they can resist cell death, in part, by transitioning into a G0/G1 cell state. Understanding how leader cells transition into (and out from) this quiescent state could offer valuable insights for developing therapeutic strategies to reduce tumor relapse caused by the re-emergence of previously dormant cells and subpopulations.^{38–40}

Our data demonstrate that subpopulations originally isolated from the same parental population exhibit fundamentally distinct responses to TGF- β 1 stimulation. We propose that this heterogeneous response is endogenously programmed within both subpopulations and is likely owed to their distinct

genetic and epigenetic profiles (Figure 2; Zoeller et al.²¹). Isolated leaders follow the canonical "go or grow" theory^{41,42} in response to TGF- β 1, exhibiting a pro-invasive phenotype with increased stress signaling, reduced proliferation, and a shift toward quiescence. However, this quiescent state is bypassed when leader cells are co-cultured with follower cells, highlighting the importance of their cooperative interaction. Additionally, while our findings align partly with the go or grow hypothesis, we demonstrate that, even within invasive subpopulations such as the leader cells, sustaining proliferation is critical for achieving macro-metastatic outgrowth. These data suggest that actively invading cells may undergo temporal shifts in proliferative status based on their position within the invasive pack, defining their primary roles in invasion processes. Additionally, we demonstrate that the regulation of cellular homeostasis—encompassing stress signaling, translation, and proliferation—depends on whether subpopulations exist in a combined heterogeneous state or independently. Whether this cooperative interplay arose by chance or by evolutionary pressures remains unknown.

Collectively, this work supports a model in which tumor cell subpopulations cooperate to maintain heterogeneity, collective invasion, and tumor progression. This cooperation includes an intercellular dialogue mediated by TGF- β 1 to promote contiguous pack formation and enhanced cellular invasion. Beyond TGF- β 1, we identify that leader cells depend on follower cells to sustain cellular proliferation in stress-inducing conditions. Overall, this study underscores the importance—and hence vulnerability—of cellular cooperation in the orchestration of collective NSCLC early invasion and metastatic disease.

Limitations of the study

We reveal that both leader and follower cells are required for maintaining subpopulation percentages and driving macro-metastatic disease in NSCLC. While our findings highlight the importance of TGF- β 1 in facilitating key processes—such as increasing pack contiguity, invasive area, and chain formation—involved in collective invasion, further investigation is required to elucidate its role in promoting pack dynamics and tumor progression *in vivo*. Additionally, we show that follower-secreted factors promote leader cell proliferation; however, further analyses are needed to resolve the specific factor(s) driving sustained leader cell proliferation in a heterogeneous cellular environment. Lastly, additional live-cell analyses are needed to understand how these processes are regulated spatiotemporally.

RESOURCE AVAILABILITY

Lead contact

Requests for further information and resources should be directed to and will be fulfilled by the lead contact, Adam I. Marcus (aimarcu@emory.edu).

Figure 7. Metastatic leader-only cells display a quiescent cellular phenotype

- (A) Two-dimensional immunofluorescence of tissue sections. $n = 5$.
- (B) Two-dimensional immunofluorescence of tissue sections. $n = 5$.
- (A and B) Scale bar, 100 μ m.
- (C) Model illustrating the findings. Created with [BioRender.com](https://biorender.com).

Materials availability

This study did not generate new unique reagents.

Data and code availability

- The single-cell RNA-seq dataset has been deposited at Sequence Read Archive as BioProject: PRJNA1183385 and is publicly available as of the date of publication.
- The proteomics sequencing dataset has been deposited at Metabolomics Workbench as PR002274: <http://dx.doi.org/10.21228/M8PN92> and is publicly available as of the date of publication.

ACKNOWLEDGMENTS

This work was supported by NIH NCI grants R01CA250422 (A.I.M.), R01CA247367 (A.I.M.), R01CA236369 (A.I.M.), PO1CA257906 (A.I.M.), R50CA265345 (J.K.M.), and an Imagine, Innovate, Impact (I3) Research award from the Emory School of Medicine through the Georgia CTSA NIH award UL1-TR002378 (A.I.M. and H.G.). Additionally, we acknowledge the following cores at Emory University for their support in this work: Integrated Cellular Imaging Core of the Winship Cancer Institute and NIH/NCI under award number 2P30CA138292-04 (RRID: SCR_023534) and Integrated Computational Core (EICC) (RRID: SCR_023525), which is subsidized by the School of Medicine and is one of the Integrated Core Facilities. Additional support was provided by the National Center for Georgia Clinical & Translational Science Alliance of the National Institutes of Health under Award Number UL1TR002378; Integrated Proteomics Core (EIPC), Shared Resource of Winship Cancer Institute and NIH/NCI under award number 2P30CA138292-04; the Pediatrics/Winship Flow Cytometry Core of Winship Cancer Institute, Children's Healthcare of Atlanta and NIH/NCI under award number P30CA138292; the Cancer Tissue and Pathology Shared Resource of Winship Cancer Institute and NIH/NCI under award number P30CA138292; Integrated Genomics Core (EIGC; RRID:SCR_023529) of the Winship Cancer Institute and NIH/NCI under award number, 2P30CA138292-04; and the Division for Animal Resources.

AUTHOR CONTRIBUTIONS

T.O.K., J.K.M., B.P., and A.I.M. conceptualized the project and designed the experiments. T.O.K., J.K.M., B.P., S.B., I.E.R., S.F.W., V.Y.M., E.R.S., G.T., and P.B. performed the experiments. T.O.K., S.B., H.R.J., J.K.M., B.P., I.E.R., L.J.M., S.F.W., and A.I.M. contributed to the bioinformatics and statistical analysis of the data. T.O.K. drafted the manuscript and designed the figures. J.K.M., A.I.M., B.P., C.M.K., P.M.V., H.M., S.F.W., and J.K. edited the manuscript. J.K.M. and A.I.M. supervised the project. J.K.M., A.I.M., and H.M. acquired project funding. All authors provided input and feedback during manuscript preparation and edited the manuscript.

DECLARATION OF INTERESTS

The authors declare no competing interests with this work.

STAR★METHODS

Detailed methods are provided in the online version of this paper and include the following:

- KEY RESOURCES TABLE
- EXPERIMENTAL MODEL SUBJECT DETAILS
 - Cell lines
 - Animal study
- METHOD DETAILS
 - Single cell Spatiotemporal Genomic and Cellular Analysis (single cell SaGA)
 - 3D Spheroid invasion assays
 - Single cell RNA sequencing
 - Variant calling
 - Immunofluorescence (IF)
 - Experimental media conditions

- Proteomics/mass spectrometry
- Immunoblotting
- Cell proliferation assay
- Flow cytometry analyses
- Quantitative PCR
- Phosphorylation array
- Hematoxylin and eosin (H&E) staining

- QUANTIFICATION AND STATISTICAL ANALYSIS

SUPPLEMENTAL INFORMATION

Supplemental information can be found online at <https://doi.org/10.1016/j.celrep.2025.115315>.

Received: March 6, 2024

Revised: November 11, 2024

Accepted: January 23, 2025

Published: February 15, 2025

REFERENCES

1. Wu, F., Fan, J., He, Y., Xiong, A., Yu, J., Li, Y., Zhang, Y., Zhao, W., Zhou, F., Li, W., et al. (2021). Single-cell profiling of tumor heterogeneity and the microenvironment in advanced non-small cell lung cancer. *Nat. Commun.* 12, 2540. <https://doi.org/10.1038/s41467-021-22801-0>.
2. Jamal-Hanjani, M., Wilson, G.A., McGranahan, N., Birkbak, N.J., Watkins, T.B.K., Veeriah, S., Shafiq, S., Johnson, D.H., Mitter, R., Rosenthal, R., et al. (2017). Tracking the Evolution of Non-Small-Cell Lung Cancer. *N. Engl. J. Med.* 376, 2109–2121. <https://doi.org/10.1056/NEJMoa1616288>.
3. Andor, N., Graham, T.A., Jansen, M., Xia, L.C., Aktipis, C.A., Petritsch, C., Ji, H.P., and Maley, C.C. (2016). Pan-cancer analysis of the extent and consequences of intratumor heterogeneity. *Nat. Med.* 22, 105–113. <https://doi.org/10.1038/nm.3984>.
4. Lawson, D.A., Kessenbrock, K., Davis, R.T., Pervolarakis, N., and Werb, Z. (2018). Tumour heterogeneity and metastasis at single-cell resolution. *Nat. Cell Biol.* 20, 1349–1360. <https://doi.org/10.1038/s41556-018-0236-7>.
5. Okamoto, T., duVerle, D., Yaginuma, K., Natsume, Y., Yamanaka, H., Kuwahara, D., Fukuda, M., Yamamoto, M., Perraudau, F., Srivastava, U., et al. (2021). Comparative Analysis of Patient-Matched PDOs Revealed a Reduction in OLFM4-Associated Clusters in Metastatic Lesions in Colorectal Cancer. *Stem Cell Rep.* 16, 954–967. <https://doi.org/10.1016/j.stemcr.2021.02.012>.
6. Keller, L., and Pantel, K. (2019). Unravelling tumour heterogeneity by single-cell profiling of circulating tumour cells. *Nat. Rev. Cancer* 19, 553–567. <https://doi.org/10.1038/s41568-019-0180-2>.
7. Baron, M., Veres, A., Wolock, S.L., Faust, A.L., Gaujoux, R., Vetere, A., Ryu, J.H., Wagner, B.K., Shen-Orr, S.S., Klein, A.M., et al. (2016). A Single-Cell Transcriptomic Map of the Human and Mouse Pancreas Reveals Inter- and Intra-cell Population Structure. *Cell Syst.* 3, 346–360.e4. <https://doi.org/10.1016/j.cels.2016.08.011>.
8. Pribluda, A., de la Cruz, C.C., and Jackson, E.L. (2015). Intratumoral Heterogeneity: From Diversity Comes Resistance. *Clin. Cancer Res.* 21, 2916–2923. <https://doi.org/10.1158/1078-0432.CCR-14-1213>.
9. Chaffer, C.L., San Juan, B.P., Lim, E., and Weinberg, R.A. (2016). EMT, cell plasticity and metastasis. *Cancer Metastasis Rev.* 35, 645–654. <https://doi.org/10.1007/s10555-016-9648-7>.
10. Hapach, L.A., Wang, W., Schwager, S.C., Pokhriyal, D., Fabiano, E.D., and Reinhart-King, C.A. (2023). Phenotypically sorted highly and weakly migratory triple negative breast cancer cells exhibit migratory and metastatic commensalism. *Breast Cancer Res.* 25, 102. <https://doi.org/10.1186/s13058-023-01696-3>.
11. Zhang, J., and Reinhart-King, C.A. (2023). Analysis of Energy-Driven Leader-Follower Hierarchy During Collective Cancer Cell Invasion.

- Methods Mol. Biol. 2608, 247–262. https://doi.org/10.1007/978-1-0716-2887-4_15.
12. Yang, Y., Zheng, H., Zhan, Y., and Fan, S. (2019). An emerging tumor invasion mechanism about the collective cell migration. Am. J. Transl. Res. 11, 5301–5312.
 13. van Zijl, F., Krupitzka, G., and Mikulits, W. (2011). Initial steps of metastasis: Cell invasion and endothelial transmigration. Mutat. Res. 728, 23–34. <https://doi.org/10.1016/j.mrrev.2011.05.002>.
 14. Friedl, P., Locker, J., Sahai, E., and Segall, J.E. (2012). Classifying collective cancer cell invasion. Nat. Cell Biol. 14, 777–783. <https://doi.org/10.1038/ncb2548>.
 15. Vilchez Mercedes, S.A., Bocci, F., Levine, H., Onuchic, J.N., Jolly, M.K., and Wong, P.K. (2021). Decoding leader cells in collective cancer invasion. Nat. Rev. Cancer 21, 592–604. <https://doi.org/10.1038/s41568-021-00376-8>.
 16. Khatib, T.O., Amanso, A.M., Knippler, C.M., Pedro, B., Summerbell, E.R., Zohbi, N.M., Konen, J.M., Mouw, J.K., and Marcus, A.I. (2023). A live-cell platform to isolate phenotypically defined subpopulations for spatial multiomic profiling. PLoS One 18, e0292554. <https://doi.org/10.1371/journal.pone.0292554>.
 17. Konen, J., Summerbell, E., Dwivedi, B., Galior, K., Hou, Y., Rusnak, L., Chen, A., Saltz, J., Zhou, W., Boise, L.H., et al. (2017). Image-guided genomics of phenotypically heterogeneous populations reveals vascular signalling during symbiotic collective cancer invasion. Nat. Commun. 8, 15078. <https://doi.org/10.1038/ncomms15078>.
 18. Commander, R., Wei, C., Sharma, A., Mouw, J.K., Burton, L.J., Summerbell, E., Mahboubi, D., Peterson, R.J., Konen, J., Zhou, W., et al. (2020). Subpopulation targeting of pyruvate dehydrogenase and GLUT1 decouples metabolic heterogeneity during collective cancer cell invasion. Nat. Commun. 11, 1533. <https://doi.org/10.1038/s41467-020-15219-7>.
 19. Pedro, B., Rupji, M., Dwivedi, B., Kowalski, J., Konen, J.M., Owonikoko, T.K., Ramalingam, S.S., Vertino, P.M., and Marcus, A.I. (2020). Prognostic significance of an invasive leader cell-derived mutation cluster on chromosome 16q. Cancer 126, 3140–3150. <https://doi.org/10.1002/cncr.32903>.
 20. Summerbell, E.R., Mouw, J.K., Bell, J.S.K., Knippler, C.M., Pedro, B., Arnst, J.L., Khatib, T.O., Commander, R., Barwick, B.G., Konen, J., et al. (2020). Epigenetically heterogeneous tumor cells direct collective invasion through filopodia-driven fibronectin micropatterning. Sci. Adv. 6, eaaz6197. <https://doi.org/10.1126/sciadv.aaz6197>.
 21. Zoeller, E.L., Pedro, B., Konen, J., Dwivedi, B., Rupji, M., Sundararaman, N., Wang, L., Horton, J.R., Zhong, C., Barwick, B.G., et al. (2019). Genetic heterogeneity within collective invasion packs drives leader and follower cell phenotypes. J. Cell Sci. 132, jcs231514. <https://doi.org/10.1242/jcs.231514>.
 22. Zhang, J., Goliwas, K.F., Wang, W., Taufalele, P.V., Bordeleau, F., and Reinhart-King, C.A. (2019). Energetic regulation of coordinated leader-follower dynamics during collective invasion of breast cancer cells. Proc. Natl. Acad. Sci. USA 116, 7867–7872. <https://doi.org/10.1073/pnas.1809964116>.
 23. Hao, Y., Hao, S., Andersen-Nissen, E., Mauck, W.M., 3rd, Zheng, S., Butler, A., Lee, M.J., Wilk, A.J., Darby, C., Zager, M., et al. (2021). Integrated analysis of multimodal single-cell data. Cell 184, 3573–3587.e29. <https://doi.org/10.1016/j.cell.2021.04.048>.
 24. Houdusse, A., and Titus, M.A. (2021). The many roles of myosins in filopodia, microvilli and stereocilia. Curr. Biol. 31, R586–R602.
 25. Brown, C.E., Warden, C.D., Starr, R., Deng, X., Badie, B., Yuan, Y.-C., Forman, S.J., and Barish, M.E. (2013). Glioma IL13R α 2 is associated with mesenchymal signature gene expression and poor patient prognosis. PLoS One 8, e77769.
 26. Garrett, S.M., Hsu, E., Thomas, J.M., Pilewski, J.M., and Feghali-Bostwick, C. (2019). Insulin-like growth factor (IGF)-II-mediated fibrosis in pathogenic lung conditions. PLoS One 14, e0225422. <https://doi.org/10.1371/journal.pone.0225422>.
 27. Hansen, A.G., Arnold, S.A., Jiang, M., Palmer, T.D., Ketova, T., Merkel, A., Pickup, M., Samaras, S., Shyr, Y., Moses, H.L., et al. (2014). ALCAM/CD166 is a TGF- β -responsive marker and functional regulator of prostate cancer metastasis to bone. Cancer Res. 74, 1404–1415. <https://doi.org/10.1158/0008-5472.CAN-13-1296>.
 28. Qi, W., Chen, X., Holian, J., Mreich, E., Twigg, S., Gilbert, R.E., and Pollock, C.A. (2006). Transforming growth factor-beta1 differentially mediates fibronectin and inflammatory cytokine expression in kidney tubular cells. Am. J. Physiol. Ren. Physiol. 291, F1070–F1077. <https://doi.org/10.1152/ajprenal.00013.2006>.
 29. Shackelford, D.B., and Shaw, R.J. (2009). The LKB1-AMPK pathway: metabolism and growth control in tumour suppression. Nat. Rev. Cancer 9, 563–575. <https://doi.org/10.1038/nrc2676>.
 30. Gilbert-Ross, M., Konen, J., Koo, J., Shupe, J., Robinson, B.S., Wiles, W.G., Huang, C., Martin, W.D., Behera, M., Smith, G.H., et al. (2017). Targeting adhesion signaling in KRAS, LKB1 mutant lung adenocarcinoma. JCI insight 2, e90487.
 31. Marcus, A.I., and Zhou, W. (2010). LKB1 regulated pathways in lung cancer invasion and metastasis. J. Thorac. Oncol. 5, 1883–1886.
 32. Zhou, W., Zhang, J., and Marcus, A.I. (2014). LKB1 tumor suppressor: Therapeutic opportunities knock when LKB1 is inactivated. Genes Dis. 1, 64–74.
 33. Ciccarese, F., Zulato, E., and Indraccolo, S. (2019). LKB1/AMPK pathway and drug response in cancer: a therapeutic perspective. Oxid. Med. Cell. Longev. 2019, 8730816.
 34. Meyuhas, O. (2015). Chapter Two - Ribosomal Protein S6 Phosphorylation: Four Decades of Research. In International Review of Cell and Molecular Biology, K.W. Jeon, ed. (Academic Press), pp. 41–73. <https://doi.org/10.1016/bs.ircmb.2015.07.006>.
 35. Chinnadurai, G., Vijayalingam, S., and Gibson, S.B. (2008). BNIP3 subfamily BH3-only proteins: mitochondrial stress sensors in normal and pathological functions. Oncogene 27, S114–S127.
 36. Ellen, T.P., Ke, Q., Zhang, P., and Costa, M. (2008). NDRG1, a growth and cancer related gene: regulation of gene expression and function in normal and disease states. Carcinogenesis 29, 2–8.
 37. Poss, K.D., and Tonegawa, S. (1997). Reduced stress defense in heme oxygenase 1-deficient cells. Proc. Natl. Acad. Sci. USA 94, 10925–10930.
 38. Recasens, A., and Munoz, L. (2019). Targeting cancer cell dormancy. Trends Pharmacol. Sci. 40, 128–141.
 39. Vallette, F.M., Olivier, C., Lézot, F., Oliver, L., Cochonneau, D., Lalier, L., Cartron, P.-F., and Heymann, D. (2019). Dormant, quiescent, tolerant and persister cells: Four synonyms for the same target in cancer. Biochem. Pharmacol. 162, 169–176.
 40. Phan, T.G., and Croucher, P.I. (2020). The dormant cancer cell life cycle. Nat. Rev. Cancer 20, 398–411.
 41. Akhmetkaliyev, A., Alibrahim, N., Shafiee, D., and Tulchinsky, E. (2023). EMT/MET plasticity in cancer and Go-or-Grow decisions in quiescence: the two sides of the same coin? Mol. Cancer 22, 90. <https://doi.org/10.1186/s12943-023-01793-z>.
 42. Serio, R.N., Scheben, A., Lu, B., Gargiulo, D.V., Patruno, L., Buckholtz, C.L., Chaffee, R.J., Jibilian, M.C., Persaud, S.G., Staklinski, S.J., et al. (2024). Clonal Lineage Tracing with Somatic Delivery of Recordable Barcodes Reveals Migration Histories of Metastatic Prostate Cancer. Cancer Discov. 14, 1990–2009. <https://doi.org/10.1158/2159-8290.CD-23-1332>.
 43. Hafemeister, C., and Satija, R. (2019). Normalization and variance stabilization of single-cell RNA-seq data using regularized negative binomial regression. Genome Biol. 20, 296. <https://doi.org/10.1186/s13059-019-1874-1>.
 44. Yu, G., Wang, L.G., Han, Y., and He, Q.Y. (2012). clusterProfiler: an R package for comparing biological themes among gene clusters. OMICS 16, 284–287. <https://doi.org/10.1089/omi.2011.0118>.

45. Erik Garrison, G.M. (2012). Haplotype-based variant detection from short-read sequencing. Preprint at arXiv. <https://doi.org/10.48550/arXiv.1207.3907>.
46. Soucek, S., Zeng, Y., Bellur, D.L., Bergkessel, M., Morris, K.J., Deng, Q., Duong, D., Seyfried, N.T., Guthrie, C., Staley, J.P., et al. (2016). The Evolutionarily-conserved Polyadenosine RNA Binding Protein, Nab2, Cooperates with Splicing Machinery to Regulate the Fate of pre-mRNA. *Mol. Cell Biol.* 36, 2697–2714. <https://doi.org/10.1128/MCB.00402-16>.
47. Seyfried, N.T., Dammer, E.B., Swarup, V., Nandakumar, D., Duong, D.M., Yin, L., Deng, Q., Nguyen, T., Hales, C.M., Wingo, T., et al. (2017). A Multi-network Approach Identifies Protein-Specific Co-expression in Asymptomatic and Symptomatic Alzheimer's Disease. *Cell Syst.* 4, 60–72.e4. <https://doi.org/10.1016/j.cels.2016.11.006>.

STAR★METHODS

KEY RESOURCES TABLE

REAGENT or RESOURCE	SOURCE	IDENTIFIER
Antibodies		
Ki-67 (8D5)	Cell Signaling Technology	Cat#9449; RRID: AB_2797703
Phospho-Histone H3 (Ser10)	Cell Signaling Technology	Cat#9701; RRID: AB_331535
Alexa Fluor 488 Phalloidin	Thermo Fisher Scientific	Cat#A12379
DAPI (4',6-Diamidino-2-Phenylindole, Dihydrochloride)	Thermo Fisher Scientific	Cat#D1306; RRID: AB_2629482
Jagged1 (D4Y1R) XP	Cell Signaling Technology	Cat#70109; RRID: AB_2799774
Jagged1 Antibody (E-12)	Santa Cruz	Cat#390177; RRID: AB_2892141
N-Cadherin (D4R1H) XP	Cell Signaling Technology	Cat#13116; RRID: AB_2687616
beta-catenin (E-5)	Santa Cruz	Cat#7963; RRID: AB_626807
MYO10	Thermo Fisher Scientific	Cat#PA5-55019; RRID: AB_2644356
IL-13RA2/CD213a2 (E7U7B)	Cell Signaling Technology	Cat#85677
Anti-TGF beta 1 [EPR21143]	Abcam	Cat#ab215715; RRID: AB_2893156
TGFBR2 Monoclonal Antibody	Proteintech	Cat#66636-1; RRID: AB_2881995
Fibronectin	Abcam	Cat#ab2413; RRID: AB_2262874
Actin	Sigma-Aldrich	Cat#A2066; RRID: AB_476693
Histone H3 (D1H2) XP	Cell Signaling Technology	Cat#4499; RRID: AB_10544537
p21 Waf1/Cip1 (12D1)	Cell Signaling Technology	Cat#2947; RRID: AB_823586
Phospho-SMAD2 (Ser465/Ser467) (E8F3R)	Cell Signaling Technology	Cat#18338; RRID: AB_2798798
SMAD2/3 (D7G7) XP	Cell Signaling Technology	Cat#8685; RRID: AB_10889933
TMEPA1/PMEPA1	LS Bio	Cat#LS-B6326; RRID: AB_11042743
PAI-1 (E3I5H) XP	Cell Signaling Technology	Cat#49536; RRID: AB_3668989
LTBP1	Proteintech	Cat#26855-1-AP; RRID: AB_2880658
Non-phospho (Active) β-Catenin (Ser45) (D2U8Y) XP	Cell Signaling Technology	Cat#19807; RRID: AB_2650576
Phospho-GSK-3B (Ser9) 5B3	Cell Signaling Technology	Cat#9323; RRID: AB_2115201
Phospho-GSK-3α/B (Ser21/9)	Cell Signaling Technology	Cat#9331; RRID: AB_329830
GSK-3α/B (D75D3)	Cell Signaling Technology	Cat#5676; RRID: AB_10547140
CD213a2 (IL13Ra2) (APC)	Miltenyi Biotec	Cat#130-128-220; RRID: AB_2928320
Anti-Jagged 1/JAG1 Antibody (PE)	Sino Biological	Cat#11648-MM03-P; RRID: AB_2860365
Ki-67 Monoclonal Antibody (SolA15), APC, eBioscience	Thermo Fisher Scientific	Cat#17-5698-82; RRID: AB_2688057
PARP (46D11)	Cell Signaling Technology	Cat#9532; RRID: AB_659884
Phospho-S6 Ribosomal Protein (Ser235/236) (D57.2.2E) XP	Cell Signaling Technology	Cat#4858; RRID: AB_2181037
S6 Ribosomal Protein (5G10) Rabbit mAb	Cell Signaling Technology	Cat#2217; RRID: AB_331355
BNIP3 (D7U1T) Rabbit mAb	Cell Signaling Technology	Cat#44060; RRID: AB_2799259
NDRG1 (D8G9) XP Rabbit mAb	Cell Signaling Technology	Cat#9485; RRID: AB_2721143
Heme Oxygenase 1 antibody	GeneTex	Cat#GTX101147; RRID: AB_1950502
LKB1 (27D10) Rabbit mAb	Cell Signaling Technology	Cat#3050; RRID: AB_823559
Phospho-AMPKa (Thr 172) (40H9) Rabbit mAb	Cell Signaling Technology	Cat#2535; RRID: AB_331250
AMPKa	Cell Signaling Technology	Cat#2532; RRID: AB_330331
GAPDH (Human Specific) Recombinant Antibody	Proteintech	Cat#80570-1-RR; RRID: AB_2918902
Phospho-eif2a (Ser51) (D9G8) XP Rabbit mAb	Cell Signaling Technology	Cat#3398; RRID: AB_2096481
Chemicals, peptides, and recombinant proteins		
TGFBR2 inhibitor, SB505124	Biotechne, Tocris	Cat#3263

(Continued on next page)

Continued

REAGENT or RESOURCE	SOURCE	IDENTIFIER
Recombinant human TGFB1	PeproTech	Cat#100-21
Collagenase/Dispase	Roche	Cat#10269638001
Halt Protease and Phosphatase Inhibitor Cocktail	Thermo Fisher Scientific	Cat#78442
SuperScript III reverse transcriptase	Invitrogen	Cat#18080-051
Critical commercial assays		
PCR-Mycoplasma Test Kit I/C	Promokine	Cat#PK-CA91-1024
Human Phospho-Kinase Array Kit	R&D systems	Cat#ARY003C
Bicinchoninic Acid Protein Assay Kit	Thermo Fisher Scientific	Cat#23225
eBioscience FOXP3/transcription factor staining buffer set	Invitrogen	Cat#00552300
RNeasy Minikit	Qiagen	Cat#74104
Deposited data		
Single Cell RNA Sequencing	This paper	SRA - BioProject: PRJNA1183385
Proteomics	This paper	Metabolomics Workbench as PR002274: http://dx.doi.org/10.21228/M8PN92
Experimental models: Cell lines		
H1915	ATCC	Cat#CRL-5904; RRID: CVCL_1505
H1299	ATCC	Cat#CRL-5803; RRID: CVCL_0600
H23	ATCC	Cat#CRL-5800; RRID: CVCL_1547
H1755	ATCC	Cat#CRL-5892; RRID: CVCL_1492
A549	ATCC	Cat#CRM-CCL-185; RRID: CVCL_0023
H1975	ATCC	Cat#CRL-5908; RRID: CVCL_1511
SKMES1	ATCC	Cat#HTB-58; RRID: CVCL_0630
Experimental models: Mouse model		
NOD.Cg-Prkdc<scid> Il2rg<tm1Wjl>/SzJ (Female)	Jackson Laboratories	RRID:IMSR_JAX:005557
Oligonucleotides		
JAG1 forward (GGCACACCTTCAACCTAAG)	Integrated Device Technology	Cat#826-1000
JAG1 reverse (TGATCATGCCGAGTGAGAAG)	Integrated Device Technology	Cat#826-1000

EXPERIMENTAL MODEL SUBJECT DETAILS

Cell lines

Human NSCLC cell lines H1299, A549, H23, H1975, H1755, and H1915 were newly purchased from the American Type Culture Collection (ATCC, Manassas, VA), cultured in RPMI 1640 media supplemented with 10% fetal bovine serum (FBS) and 1% penicillin-streptomycin (P/S), and incubated at 37°C and 5% CO₂. Similarly, the SKMES1 human NSCLC cell line was also obtained from ATCC, cultured in EMEM medium supplemented with 10% FBS and 1% P/S, and incubated at 37°C and 5% CO₂. Leader and follower subpopulations were derived from H1299 parental cells transfected with palmitoylated dendra2 (pal-dendra2) and isolated via the SaGA method as previously described.^{16,17} H1299, Leader, Follower, H23, A549, and SKMES1 cell lines were male. H1975, H1755, and H1915 cell lines were female. All cell lines were passaged at 70% confluence and both adherent and nonadherent cells were collected at each passage. Media was replenished every two days. All cell lines tested negative for mycoplasma contamination using a commercially available kit (PCR-Mycoplasma Test Kit I/C, Promokine PK-CA91-1024) before experimentation.

Animal study

All animal studies were approved by Emory University's Institutional Animal Care and Use Committee (IACUC). Female NSG mice (strain JAX 005557 NOD.Cg-Prkdc<scid> Il2rg<tm1Wjl>/SzJ), were obtained from Jackson Laboratories and randomly divided with 5 mice per cage. Mice aged approximately 7–8 weeks were injected subcutaneously in the right flank with 1 million cells each, 5–10 mice per experimental group. Tumor burden (20 mm) was matched at mouse endpoint. Weekly assessments were performed in accordance with the body condition scoring system (BDS) as outlined by Emory's Division of Animal Resources. Mice were monitored weekly to assess, BDS, tumor volume, and mouse weight. Macro/micro lesion size criteria was established with the aid of a veterinary pathologist.

METHOD DETAILS

Single cell Spatiotemporal Genomic and Cellular Analysis (single cell SaGA)

Single cell SaGA is a modified version of the SaGA technique¹⁶ wherein single cells are selected based upon live phenotypic criteria to be sorted and immediately submitted for single-cell RNA sequencing. Briefly, H1299 NSCLC spheroids, stably expressing pal-dendra2, were embedded in a basement membrane matrix and allowed to invade for 48 H. Using a confocal microscope equipped with live-cell imaging, scanning-photoconversion modes, and multi-wavelength lasers (405, 488, and 568 nm), we photoconverted collectively invading cells. As previously described,¹⁷ H1299 spheroids contained approximately 5–10 collective invasion packs per spheroid, with approximately 6–20 cells per pack. To account for cell loss during retrieval steps, we estimate 8–12 spheroids were used for photoconversion. After matrix degradation utilizing Collagenase/Dispase (Roche, 10269638001), a single-cell suspension was achieved, and cells were sorted using fluorescence-activated cell sorting (FACS) into a 96-well plate for immediate single-cell RNA sequencing and downstream analysis.

3D Spheroid invasion assays

Spheroids were generated utilizing 3000–5000 cells/spheroid as previously described¹⁶ and embedded into 5 mg/mL Matrigel basement membrane matrix contained within a 14 mm microwell where the bottom surface is a No. 1.5 coverglass (Corning, 356237 and Mattek P35G-1.). Imaging was performed using the Olympus CKX41 microscope with Infinity 1-3C camera (x4 air, 0.13 numerical aperture (NA), UPlanFL N). We quantified invasive surface area, spheroid circularity, and number of chains using ImageJ as previously described.¹⁶ Raw images were post-processed in Adobe Illustrator using the ‘glowing edges’ stylize effect. A modified culture medium containing 5% FBS and 1% P/S was utilized for 3D culture, except for H1975 cells, which were maintained in standard media.

Single cell RNA sequencing

A total of 164 H1299 cells involved in collective invasion were processed for single-cell RNA sequencing and 111 cells yielded quality RNA sequencing data. Cells were deposited into 10 mL RNeasy lysis (RLT) buffer (Qiagen, 79216) in separate wells of a 96-well plate. RNA library preparation and sequencing were carried out by the EPC Genomics Core. Data processing, read alignment, and quality control were performed by the Emory Integrated Computational Core. The feature count matrix was processed and analyzed using R v4.2.1 and the Seurat package v4.3.0.²³ The Seurat SCTransform method was employed for normalization and variance stabilization of molecular count data.⁴³ During the SCTransform step, differences in the number of features and UMIs were regressed out. Clustering was completed by using the RunPCA(), FindNeighbors(), and FindClusters() functions with the first 30 principal components and a clustering resolution of 0.8. Nonlinear dimensionality reduction was performed using t-distributed Stochastic Neighbor Embedding (tSNE) technique with the RunTSNE() function implemented in Seurat package. The cell cycle phases were assigned to the cells with CellCycleScoring() function. The differential expression analysis was done by applying the FindMarkers() function in Seurat, utilizing the default Wilcoxon Rank-Sum test. The gseGO() function from the clusterProfiler package v4.7.1 was used for gene set enrichment analysis.⁴⁴

Variant calling

Variant calling within raw single cell RNAseq data was performed by the Emory EPC Genomics Core utilizing the haplotype-based variant detector, Freebayes, designed to find small polymorphisms.⁴⁵ (<https://github.com/ekg/freebayes>). Gene selection was based on the previously established leader and follower mutation profiles from our previous work.²¹ The cutoff for each gene was determined by single cell RNA sequence coverage and reads for each individual cell. Genes without full coverage across all cells were excluded from the classification criteria. Additionally, single cells harboring mutations associated with both leader and follower cells have been classified as “both”.

Immunofluorescence (IF)

3D: Spheroids were fixed on day two of invasion with prewarmed 4% paraformaldehyde (PFA) for 40 min at room temperature with gentle agitation and then subjected to three 5 min washes with IF buffer (3.5 mM NaH2PO4, 130 mM NaCl, 7 mM NaH2PO4, 0.4%, Triton X-100, 0.05% Tween 20, filter sterilized). Blocking was performed with 3% normal goat serum (NGS) in IF buffer for 30 min at room temperature, followed by overnight incubation with primary antibody at room temperature. The next day, spheroids were washed with IF buffer and then subsequently stained with secondary antibody for 2 h at room temperature. Following three 10 min washes, imaging was conducted on the Leica TCS SP8 inverted confocal microscope (x20 air HC PL APO CS2, 0.75 NA and x63 oil HC PL APO CS2, 1.4 NA) using line scanning (405-nm direct modulation Flexible, 488-nm argon, 561-nm diode pumped solid-state, and 633-nm helium-neon), 4x line averaging, and both Hyd GaAsP and photomultiplier tube detectors. FIJI ImageJ was employed for image analysis and quantification. When applicable, phalloidin brightness was adjusted in the vehicle-treated samples to match the fluorescence intensity observed upon TGFB1 stimulation.

2D: Paraffin embedded tissue sections were deparaffinized by incubation with xylene, followed by rehydration using a series of decreasing ethanol concentrations in water. After antigen retrieval, blocking was performed with 5% NGS in IF buffer for 10 min at room temperature. The samples were then incubated with primary antibody in 20% block in IF buffer overnight at 4°C in a

humidified chamber, washed, and subsequently incubated with secondary antibody for 1 H. After additional washes and a 20 min incubation in PBS, samples were fixed with Prolong Diamond and imaged using the Olympus IX51 inverted microscope (20x air LUC PLAN FL N, 0.45 NA) using epi-fluorescence.

Experimental media conditions

In all 2D experiments, cells were initially seeded in standard media conditions (10% FBS, 1% P/S in respective media). The media was replaced the following day to reflect specific experimental conditions after rinsing cells twice with 1X PBS. For sustained 48 h treatment experiments, media was switched to a defined media composition [1X insulin-transferrin-selenium-ethanolamine, 0.5 mg/mL hydrocortisone, 1 ng/mL cholera toxin, 50 nM O-phosphorylethanolamine, and 5 nM triiodothyronine] in appropriate media and additional treatments. Time course and 30 min acute stimulation experiments were performed by replacing the media with 100% RPMI 1640 followed with timed treatments after 24 h. 8-day TGFB1 treatment was performed in 2.5% FBS in 100% RPMI to support long-term leader cell proliferation. All experiments were seeded to reach 70% confluence by endpoint. For experiments treated with conditioned defined media, conditioned defined media was harvested 48 h after incubation with follower cell subpopulation.

Proteomics/mass spectrometry

LC-MS/MS was performed on the secreted media content of adherent leader and follower cell populations in 2D culture. Cells were initially cultured in standard media for 24 h and then replaced with defined media after two rinses with 1X PBS. After 48 H, the media was collected and centrifuged at 250 g for 5 min to remove any detached cells, followed by a 20 min centrifugation at 2000 g to eliminate apoptotic bodies. The media was then concentrated using the Amicon ultra-15 centrifugal filter unit with a 3-kDa cut off and centrifugation at 4000 g at 4°C for a final volume of 250 mL. Samples were flash-frozen before storage at -80°C. Protein normalization, digestion, and LC-MS/MS data acquisition and analysis were conducted at the Emory Integrated Proteomics Core using the Orbitrap Fusion Lumos Mass Spectrometer with 120,000 resolution, 400 to 1600 m/z range, 400,000 automatic gain control (AGC), 246 ms max injection time and rf lens at 30%.^{46,47} Experiment was conducted across four biological replicates.

Immunoblotting

Cell lysis was performed using a 2% SDS lysis buffer [2% SDS, 50 mM tris (pH 8.0), and 100 mM NaCl] supplemented with Halt Protease and Phosphatase Inhibitor Cocktail (Thermo Fisher Scientific, 78442). Detached cells in the spent culture medium were collected and mixed with the sample after centrifugation at 250 g for 5 min at room temperature. After brief sonication, sample protein concentrations were determined using Bicinchoninic Acid Protein Assay kit (Thermo Fisher Scientific, 23225). Whole cell lysate (WCL) protein samples were then normalized for equal loading, reduced, and denatured before undergoing SDS-PAGE. The conditioned defined media (CM) samples were processed similarly to proteomics mass spectrometry samples to concentrate the secreted proteins for SDS-PAGE. CM protein content was quantified as described above. Standard immunoblotting procedures were followed. Membranes were developed using the ChemiDoc Imaging system. Densitometry analysis was performed using FIJI ImageJ.

Cell proliferation assay

Cells were seeded at 20% confluence in 6-well plates, (one well per day, per condition) and counted over five consecutive days. Detached and trypsinized cells were combined and centrifuged at 250 g for 5 min at room temperature. After cell suspension, trypan blue staining was conducted using the Denovix Cell Drop Brightfield Cell Counter. Defined media with and without TGFB1 was refreshed daily, and data were normalized to the cell count 24 h post-seeding. The experiment was conducted across three biological replicates.

Flow cytometry analyses

Flow cytometry experimental setup mirrored the sustained 48 h treatment conditions. Both detached and adherent cells, the latter harvested by trypsinization, were pooled and centrifuged at 250 g for 5 min. For live cell staining analysis and sorting, cells were washed once with 1X PBS, followed by staining for 30 min at 4°C with agitation in the dark using 5% dialyzed FBS in phenol-red-free RPMI 1640. Cells were then washed twice, resuspended in the same flow buffer, and analyzed. Intracellular staining was performed post-fixation and permeabilization using the eBioscience FOXP3/transcription factor staining buffer set (Invitrogen, 00552300) according to the manufacturer's instructions. For live and intracellular flow cytometry experiments, analysis was performed using the BD FACSYMPHONY A3 system with the BD FACSDiva software. Cells were sorted using the BD FACSaria II Flow Cytometry Cell Sorter. All subsequent analysis and quantification were performed using FlowJO and GraphPad Prism.

Quantitative PCR

After a 48 h period of sustained treatment, cells were lysed using RLT Buffer with a 1% addition of B-mercaptoethanol (BME). Subsequently, RNA was extracted and purified utilizing the RNeasy Minikit (cat. num. 74104). 1 µg RNA was reverse transcribed with 50 ng random hexamers and 200 U of Invitrogen SuperScript III reverse transcriptase (cat. num. 18080-051). RT-qPCR was performed using Applied Biosystems PowerUP SYBR Green Mastermix (cat. num. A25780) on the BioRad CFX Opus 96 Real-Time PCR system. Expression levels were calculated using the $2^{-\Delta\Delta Ct}$ method and normalized to YWHAZ RNA expression. Primer sequences

for all qPCR reactions are JAG1 forward (GGCAACACCTTCAACCTCAAG), JAG1 reverse (TGATCATGCCGAGTGAGAAG), YWHAZ forward (ACCGTTACTTGGCTGAGGTTGC), and YWHAZ reverse (CCCAGTCTGATAGGATGTGTTGG).

Phosphorylation array

Cells prepared for phosphorylation array were subjected to a 24 h starve in 100% RPMI followed by a 30 min acute stimulation. Samples were then processed using the Human Phospho-Kinase Array Kit (R&D systems, ARY003C) according to the manufacturer's guidelines. Nutrient deprivation was performed to provide a stable baseline (in the absence of serum derived factors) to assess, with the addition of TGFB1, maximal growth factor stimulation within the leader and follower subpopulations. The membranes were developed using the ChemiDoc Imaging system. The phosphorylation array was replicated across three biological samples.

Hematoxylin and eosin (H&E) staining

At the conclusion of the study, primary tumor tissue along with lungs, liver, brain, and kidneys from the mice were harvested and fixed in 4% formalin for 24 H, then transferred to 70% ethanol. These prepared tissues were then submitted to the Emory Cancer Tissue and Pathology Core for processing and H&E slide preparation.

QUANTIFICATION AND STATISTICAL ANALYSIS

Experimental quantification and statistical analyses were performed using the tests specified in the figure legends, following validation of data adherence to relevant assumptions (normal distribution, uniform variance, and independent sampling). Biological replicates are denoted as 'n' and technical replicates as 'N'. All reported *p* values are two-tailed, and bar graph representations depict means with SD error bars (unless otherwise noted). Statistical analyses were performed using Microsoft Excel, FIJI ImageJ, and GraphPad Prism software. Significance was determined at *p* < 0.05.